Atmos. Chem. Phys., 23, 9685–9723, 2023
https://doi.org/10.5194/acp-23-9685-2023

Atmospheric Chemistry and Physics
Open Access
EGU

Atmospheric CO_2 inversion reveals the Amazon as a minor carbon source caused by fire emissions, with forest uptake offsetting about half of these emissions

Luana S. Basso[1,2,3], Chris Wilson[4,5], Martyn P. Chipperfield[4,5], Graciela Tejada[2], Henrique L. G. Cassol[2,6], Egídio Arai[2], Mathew Williams[6], T. Luke Smallman[6], Wouter Peters[7,8], Stijn Naus[7,9], John B. Miller[10], and Manuel Gloor[1]

[1]School of Geography, University of Leeds, Leeds, LS2 9JT, UK
[2]General Coordination of Earth Science (CGCT), National Institute for Space Research (INPE), São José dos Campos, Brazil
[3]Department of Biogeochemical Signals, Max Planck Institute for Biogeochemistry, Jena, Germany
[4]School of Earth and Environment, University of Leeds, Leeds, LS2 9JT, UK
[5]National Centre for Earth Observation, University of Leeds, Leeds, LS2 9JT, UK
[6]School of GeoSciences and National Centre for Earth Observation, University of Edinburgh, Edinburgh, EH9 3FF, UK
[7]Environmental Sciences Group, Wageningen University and Research, 6708PB, Wageningen, the Netherlands
[8]University of Groningen, Centre for Isotope Research, 9747AG, Groningen, the Netherlands
[9]Earth, SRON Netherlands Institute for Space Research, 2333CA, Leiden, the Netherlands
[10]NOAA – Global Monitoring Laboratory, Boulder, Colorado 80305, USA

Correspondence: Luana S. Basso (luanabasso@gmail.com, lbasso@bgc-jena.mpg.de)

Received: 5 January 2023 – Discussion started: 25 January 2023
Revised: 12 May 2023 – Accepted: 28 May 2023 – Published: 1 September 2023

Abstract. Tropical forests such as the Amazonian rainforests play an important role for climate, are large carbon stores and are a treasure of biodiversity. Amazonian forests have been exposed to large-scale deforestation and degradation for many decades. Deforestation declined between 2005 and 2012 but more recently has again increased with similar rates as in 2007–2008. The resulting forest fragments are exposed to substantially elevated temperatures in an already warming world. These temperature and land cover changes are expected to affect the forests, and an important diagnostic of their health and sensitivity to climate variation is their carbon balance. In a recent study based on CO_2 atmospheric vertical profile observations between 2010 and 2018, and an air column budgeting technique used to estimate fluxes, we reported the Amazon region as a carbon source to the atmosphere, mainly due to fire emissions. Instead of an air column budgeting technique, we use an inverse of the global atmospheric transport model, TOMCAT, to assimilate CO_2 observations from Amazon vertical profiles and global flask measurements. We thus estimate inter- and intra-annual variability in the carbon fluxes, trends over time and controls for the period of 2010–2018. This is the longest period covered by a Bayesian inversion of these atmospheric CO_2 profile observations to date. Our analyses indicate that the Amazon is a small net source of carbon to the atmosphere (mean 2010–2018 $= 0.13 \pm 0.17\,\mathrm{Pg\,C\,yr^{-1}}$, where 0.17 is the 1σ uncertainty), with the majority of the emissions coming from the eastern region (77 % of total Amazon emissions). Fire is the primary driver of the Amazonian source ($0.26 \pm 0.13\,\mathrm{Pg\,C\,yr^{-1}}$), while forest carbon uptake removes around half of the fire emissions to the atmosphere ($-0.13 \pm 0.20\,\mathrm{Pg\,C\,yr^{-1}}$). The largest net carbon sink was observed in the western-central Amazon region (72 % of the fire emissions). We find larger carbon emissions during the extreme drought years (such as 2010, 2015 and 2016), correlated with increases in temperature, cumulative water deficit and burned area. Despite the increase in total carbon emissions during drought years, we do not observe a significant trend over time in our carbon total, fire and net biome exchange estimates between 2010 and 2018.

Published by Copernicus Publications on behalf of the European Geosciences Union.

Our analysis thus cannot provide clear evidence for a weakening of the carbon uptake by Amazonian tropical forests.

1 Introduction

The uptake of carbon dioxide (CO_2) by plants helps to mitigate global climate change. The land carbon sink is estimated to have offset approximately 25 % of all fossil fuel emissions since 1960 (Friedlingstein et al., 2020). Tropical forests, like those in Amazonia, are the largest in the world and have historically been a major component of this land carbon sink. Measurements of aboveground biomass changes indicate an increase in Amazonian old-growth forest biomass over time, summing to a total sink of 0.38 (0.28–0.49 95 % C.I.) Pg C yr^{-1} in the 2000s (Brienen et al., 2015). However, the Amazon carbon cycle is affected by both direct (deforestation and degradation) and indirect (climate change) anthropogenic forest disturbances, as the reduction in the forest carbon uptake capacity during drought years (Phillips et al., 2009; Gatti et al., 2014; van der Laan-Luijkx et al., 2015; Alden et al., 2016). A decline in the Amazon carbon accumulation was observed over 1983 to mid-2011, as a consequence of an increase in tree mortality throughout this period, possibly as a result of greater climate variability and feedbacks of faster growth on mortality, resulting in shortened tree longevity (Brienen et al., 2015).

Human-induced land use and cover change, and forest degradation (driven by fires caused by anthropogenic activity in association with drier conditions and logging), are the main direct disturbances in the Amazon forest (Fawcett et al., 2023; Lapola et al., 2023). These disturbances have been estimated to result in aboveground biomass losses of 1.3 (±0.4) Pg C (between 2012 and 2019; Fawcett et al., 2023). Kruid et al. (2021) attributed 56 % of the carbon loss in this region during the period from 2003 to 2019 to deforestation, with the remainder (44 %) to forest degradation and disturbance (including fire, natural disturbances, drought-induced tree mortality, edge effects, selective logging and other extractive activities). Over the past 40 years, the Amazon forest area has decreased by 17 % (MapBiomas, 2022), and degradation (between 1995 and 2017) accounts for around 17 % of total forest area (Lapola et al., 2023). Forest fires are associated with a combination of human activities providing the ignition source and climatic factors which create drier and hotter conditions (Ray et al., 2005). Tropical forests like those in Amazonia are rarely susceptible to natural fires. In general, the forest fires observed in this region result from the leakage of fires from deforested areas to adjacent forests (Aragão et al., 2018). In addition, deforestation and selective logging promote degradation of adjacent forests, increasing their vulnerability to fires, which could result in further degradation (Aragão et al., 2018). Silva et al. (2020) found that forest fires affect the Amazon forest carbon cycle for at least 30 years after the fires, with just 35 % of this emission being compensated for by cumulative CO_2 uptake of burned forests during this period.

As climate change continues, extreme climate events across the Amazon region have become increasingly common (Gloor et al., 2013). Recently, a warming trend in Amazonian annual mean temperature over the last 40 years was reported, where the eastern and mainly southeastern regions showed stronger trends than the global mean trend (Gatti et al., 2021a). The largest increases in Amazon temperature were observed for the dry season months, in addition to a decrease in precipitation of 17 % during these months, strongly enhancing the contrast between the dry and wet seasons (Gatti et al., 2021a; Haghtalab et al., 2020). The Amazon is estimated to have suffered a substantial carbon loss due to fires caused by the 2015–2016 El Niño drought and heat wave in the eastern Amazon; long-term forest plot monitoring reveals that carbon losses remained elevated for up to 3 years (Berenguer et al., 2021). These impacts could have been amplified by human disturbance, which means that human-modified forests may be more susceptible and sensitive to fires (Berenguer et al., 2021).

Recently, Gatti et al. (2021a) reported new top-down estimates of the Amazon carbon balance covering the period 2010–2018. The Amazonian carbon balance is of interest for two reasons: first to understand how tropical forest productivity and losses fit in the global carbon balance, specifically the substantial global land sink, and second as an indicator of Amazonian forest performance changes over time. Gatti et al. (2021a) found a net carbon release to the atmosphere of 0.29 ± 0.40 Pg C yr^{-1}, including 0.41 ± 0.05 Pg C yr^{-1} of fire emissions. The net biome exchange (NBE, representing the balance between photosynthesis, respiration and decomposition and excluding fire) compensated for 31 % of fire emissions from the atmosphere, yielding a small NBE sink for Amazonia of -0.12 ± 0.40 Pg C yr^{-1} (Gatti et al., 2021a). In addition, Gatti et al. (2021a) reported an east–west difference in total flux mainly related to fire emissions but also highlighted that the southeastern Amazon region acts as a net carbon source (total carbon flux minus fire emissions) to the atmosphere. The authors suggest that the historical land use change and the strong climate trends (the temperature increase and decrease in precipitation mainly during the dry season) observed in this southeast region may explain the positive NBE (i.e., a source of C to the atmosphere) in the southeast, as its estimated positive trend suggests that increasing temperatures and decreasing soil water availability

have a significant impact on the vegetation carbon balance, at least in southeast Amazonia (Gatti et al., 2021a).

These estimates were based on 9 years of lower-troposphere vertical CO_2 and CO profile observations and an air column mass balance technique to estimate fluxes. In essence, the fluxes are estimated as the difference between the air column CO_2 content at the site and the location where air enters the Amazon on its path to the site divided by the air travel time from the coast to the site (Gatti et al., 2021a; Miller et al., 2007). Estimates based on this approach have uncertainties. For example, we assume well-mixed conditions during the sampling. As reported by the authors, the approach does not account for convective process that may result in losses of surface flux CO_2 at the top of the profiles (typically 4.5 km a.s.l.) (Gatti et al., 2021a). There are also uncertainties in the estimates of background air concentrations (as it is assumed that remote Atlantic marine boundary layer concentrations represent the partial column entering the coast; Domingues et al., 2020; Gatti et al., 2021a), and we also do not account for diurnal cycles in NBE that may impact the partial column mean CO_2.

In order to extract Amazonian surface flux information from the vertical profiles using an independent approach, we apply a global three-dimensional (3-D) Eulerian offline chemical transport model, TOMCAT (Chipperfield, 2006), and its inverse model, INVICAT (Wilson et al., 2021), to atmospheric CO_2 data. We estimate Amazonian surface fluxes between 2010 and 2018 using the CO_2 observations from global surface monitoring sites (Lan et al., 2022) and lower-troposphere vertical profiles in Amazonia (Gatti et al., 2021a). As this 3-D transport model is global and simulates convective cloud transport processes, some of the uncertainties are reduced compared to the air column budgeting method. To the best of our knowledge the complete 2010–2018 Amazonian vertical profile dataset has not yet been used in 3-D atmospheric transport inversions. INVICAT uses a variational scheme, based on 4D-Var methods used in numerical weather prediction (NWP) (e.g., Le Dimet and Talagrand, 1986), to minimize the difference between predicted and observed dry-air mole fractions. Using this methodology, we quantify fluxes and analyze their seasonal patterns, interannual variability and trends for Amazon. We also estimate carbon emissions from fires to constrain the Amazon carbon budget using flux estimates from an independent global inverse modeling based on atmospheric carbon monoxide (CO) measured from space and relate the carbon fluxes (total, fire and NBE) to climate controls. In Sect. 2 we describe the inverse modeling approach and describe the observations used; in Sects. 3 and 4 we discuss our results, analyze the drivers of CO_2 fluxes (as in cumulative water deficit, temperature, solar radiation and burned area), cross-validate our model mole fractions with independent Amazon observations and compare our estimates with other previous published Amazonian estimates, mainly with estimates using an air column mass balance technique. Finally, we summarize the extent to which our results are in agreement with previous Amazon carbon flux estimates.

2 Methods

2.1 Observations

We assimilate in situ surface flask observations from global surface observation sites and Amazonian lower-troposphere vertical profiles of CO_2 into the TOMCAT inverse atmospheric transport model for a 9-year period between 2010 and 2018.

2.1.1 Amazonian aircraft profiles

We assimilated CO_2 observations from 590 lower-troposphere vertical profiles over five sites in the Brazilian Amazon (Santarem, SAN: 55.0° W, 2.9° S; Tabatinga, TAB: 69.7° W, 6.0° S; Alta Floresta, ALF: 56.7° W, 8.9° S; Rio Branco, RBA: 67.9° W, 9.3° S; Tefe, TEF: 66.5° W, 3.6° S; Fig. 1). Air samples were collected approximately twice per month aboard light aircraft from 4.4 to 0.3 km a.s.l. using automatic samplers between 2010 and 2018 (see Gatti et al., 2021a, for more details). All samples were collected between 12:00 and 13:00 local time (LT), when the boundary layer is fully developed and most likely to be well mixed. Samples were measured for CO_2 and CO mole fraction with high accuracy and precision at the greenhouse gas laboratory at the National Institute of Space Research (LaGEE/INPE), Brazil (Gatti et al., 2021a, 2014). For the inversions we used the mean concentration of each vertical profile in the planetary boundary layer (PBL) level (below 1.5 km a.s.l., levels with higher influence of the surface flux in the concentrations) and the vertical profile free-troposphere mean (above 3.5 km a.s.l., levels with lower influence of the surface flux in the concentrations, better representing the background concentrations). The vertical profile data used here are available at PANGAEA Data Archiving at https://doi.org/10.1594/PANGAEA.926834 (Gatti et al., 2021b).

Recently, the National Oceanic and Atmospheric Administration's Global Monitoring Laboratory (NOAA GML) have found that the CO_2 concentration is artificially reduced when air samples with high ($> 1.7\,\%$) water vapor are pressurized in PFP (programmable flask package) flasks to 2.7 bar, as a result of condensation (Baier et al., 2020). The LaGEE system has some differences from the NOAA system, and, as reported by Gatti et al. (2022), a preliminary study using vertical profiles near Manaus (Amazonas state, Brazil) compared PFP samples measured for CO_2 at LaGEE/INPE to onboard measurements from a trace gas flight analyzer largely immune to water effects (Picarro model G2401-m) and found depletions in PFP CO_2 similar to those from the Baier et al. (2020) study. They also report that this influence is likely greatest near the surface, as hu-

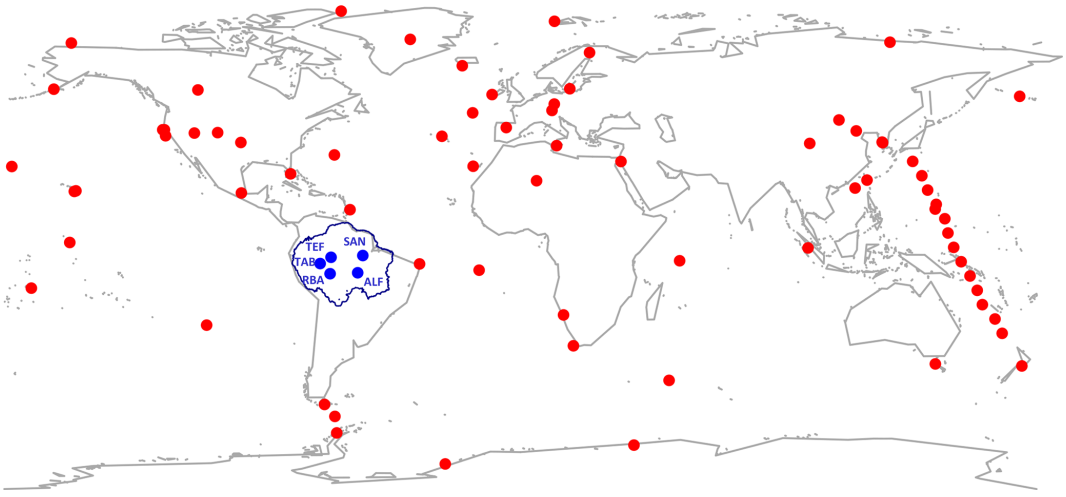

Figure 1. Locations of LaGEE/INPE Amazon vertical profile sites (blue circles) and NOAA surface sites from which flask-based measurements of CO_2 are assimilated (red circles). The blue contour represents the Amazon area, based on Eva and Huber (2005).

midity increases towards lower altitudes, which means that true CO_2 in the lower half of the profiles may be higher than measured (Gatti et al., 2022), meaning that our current fluxes to the atmosphere presented here could be underestimated.

2.1.2 Surface flask observations

To estimate carbon fluxes, we also assimilated CO_2 global long-term surface data provided by the NOAA GML (https://doi.org/10.15138/wkgj-f215, Lan et al., 2022) into the inverse model. Data from a total of 72 monitoring sites were used, where air samples in flasks are collected weekly to biweekly (Fig. 1, Table A1). These measurements have high accuracy (~ 0.2 ppm), and most of the sites are located in the Northern Hemisphere. There are few monitoring sites in tropical regions, which increases the uncertainties of regional estimates in the tropics. Here, we reduce these uncertainties for Amazonia with the inclusion of the lower-troposphere vertical profile data.

2.2 Model setup

2.2.1 Inverse model setup

To estimate the net carbon flux between Amazon and the atmosphere we use the inverse of the atmospheric transport model TOMCAT (Chipperfield, 2006). TOMCAT is a global 3-D Eulerian offline atmospheric chemistry and air constituent transport model, which has previously been used to estimate greenhouse gas emissions (e.g., Wilson et al., 2016, 2021; Gloor et al., 2018). The INVICAT inversion framework (Wilson et al., 2014) used is based on the TOMCAT model and its adjoint. A detailed description of the TOMCAT model and the 4D-Var inverse method employed by INVICAT is presented in Chipperfield (2006) and Wilson et al. (2014), respectively. A previous study with simulations of sulfur hexafluoride (SF_6) and other species comparing different transport models investigated some of the large-scale transport characteristics (Patra et al., 2011) and shows that TOMCAT in general performed well, slightly overestimating the SF_6 inter-hemispheric gradient compared to observations but within the bounds of other transport models.

The forward and adjoint model simulations were carried out globally at $5.6° \times 5.6°$ horizontal resolution, with 60 vertical levels up to 0.1 hPa. Although we did not investigate the uncertainties of the coarse resolution in our estimates, previous CH_4 inversion estimates using the TOMCAT model with inversions at 2.8 and 5.6° resolution and assimilating GOSAT data showed that the results were robust at both resolutions (Wilson et al., 2021). The inversions were carried out for each year separately and each completed 50 minimization iterations. In order to better constrain fluxes during the final months of each year, the inversion for each year was actually run for 16 months, from December of the previous year to the end of March for the following year, with the first month and the final 3 months being discarded from the results, and each inversion was initialized using 3-D fields provided from the correct date in the previous year. The model meteorology (including winds, temperature and pressure data) was taken from the European Centre for Medium-Range Weather Forecasts (ECMWF) ERA-Interim reanalysis (Dee et al., 2011).

The initial conditions for the inversions come from prior CO_2 simulations and inversions which began in 1995. For those simulations the initial conditions were included within the state vector and optimized in order to produce an initial global 3-D field consistent with observations. For the assimilated observation data from both surface monitoring sites and the vertical profile sites, the model output was linearly interpolated to the correct longitude, latitude and altitude at the nearest model time step. In addition, uncorrelated random errors of 1 ppm were attributed to each observation. In ad-

dition, representation uncertainty for each observation was calculated online during the model simulation as the mean difference across the six model grid cells adjacent (2 in z, 2 in x and 2 in y direction) to that containing the observation location. The random and representation errors were then combined in quadrature to provide the overall observation uncertainty.

In addition to atmospheric CO_2 mole fractions, a priori monthly mean flux values for each grid cell along with a diagonal error covariance matrix for these values were used as input for the inversion calculation. A priori grid cell uncertainties were assumed to be uncorrelated. The result of the inversion is an a posteriori estimate of monthly mean grid cell fluxes and an error covariance matrix. Using TOMCAT, we ran forward a priori and a posteriori flux estimates to simulate atmospheric CO_2 air mole fractions. Here we will refer to the mean a priori and a posteriori fluxes as "prior fluxes" and "posterior fluxes" and the a priori and a posteriori mole fractions as "prior mole fractions" and "posterior mole fractions". In our CO_2 inversion estimate, fossil fuel flux was fixed and land–biosphere, ocean and fire emissions were optimized. Prior emissions are given grid cell uncertainties of 308 % of the prior flux value to give a total global uncertainty based on the Global Carbon Project (Friedlingstein et al., 2020) of $1.7\,\mathrm{Pg\,C\,yr^{-1}}$, with a different uncertainty value attributed to land and ocean grid cells. The differentiation was based on assuming the Global Carbon Project (Friedlingstein et al., 2020) total uncertainty estimates of 1.1 and $0.6\,\mathrm{Pg\,C\,yr^{-1}}$ for land and ocean global flux uncertainties, respectively.

To derive the uncertainties for the posterior emissions, we followed the approach described by Wilson et al. (2021), where estimates for each year's posterior emission covariance error matrix using cost function gradient values were produced from the limited-memory Broyden–Fletcher–Goldfarb–Shanno algorithm (L-BFGS). We use this to minimize the cost function (Nocedal, 1980), based on the method suggested by Bousserez et al. (2015). Considering that this iterative method estimates the inverse of the Hessian (the second derivative) of the cost function and the off-diagonal elements of the posterior covariance matrix are not included, the posterior errors included here are estimates, with their own remaining uncertainties (Bousserez et al., 2015).

2.2.2 Prior flux estimates

Prior flux estimates include three components and were taken from available bottom-up models and inventories. Fossil fuel emissions are taken from the CDIAC inventory (Boden et al., 1999) and vary each year up to 2016, after which they were scaled to Global Carbon Budget values obtained from Friedlingstein et al. (2020). For estimates of air–sea fluxes we used a combination of Takahashi et al. (2009) and Khatiwala et al. (2009), following the methodology described by Gloor et al. (2018), and they were scaled to the Global Carbon Budget values (Friedlingstein et al., 2020). For the monthly land–biosphere fluxes (net land gains or losses) we used an annually repeating and balanced land vegetation–atmosphere CO_2 flux from the Carnegie–Ames–Stanford Approach (CASA) Global Fire Emissions Database (GFED4) land–biosphere model (Potter et al., 1993; Randerson et al., 2017), an average climatology for 2003–2013. We did not change the land–biosphere prior annually because we preferred the interannual variations to be informed by the atmospheric observations. In the CASA model, primary productivity is predicted using the relationship between greenness reflectance properties, the fraction of absorption of photosynthetically active radiation (fPAR) and a light utilization efficiency term, where the canopy greenness is measured using a normalized difference vegetation index (NDVI) that is computed from the ratio of visible and near-infrared radiation reflected from the canopy as detected by the AVHRR satellite sensor (Potter, 1999).

To evaluate the influence of the Amazon vertical profile data on flux estimates, we have also performed an inversion without the profile data, using only the NOAA surface data. The latter approach was shown previously to induce large biases in the estimated Amazonian fluxes, resulting from a lack of tropical constraints (van der Laan-Luijkx et al., 2015) and an overestimated tropical-NH dipole (Stephens et al., 2007). For simplicity, here we will call the posterior fluxes from the inversion using the Amazon vertical profile data and the inversions without that data "posterior total flux (with Amazon observations)" and "posterior total flux (without Amazon observations)", respectively.

To evaluate the influence of the biosphere prior on flux estimates, we compare our inversions using the CASA model as land–biosphere prior flux with inversions, using the carbon data model framework (CARDAMOM) (Bloom et al., 2016) as land–biosphere prior flux for South America with $1^\circ \times 1^\circ$ spatial and monthly temporal resolutions between 2001 and 2017 (inclusive). CARDAMOM is a Bayesian calibration system that generates diagnostic estimates of the terrestrial C cycle (pools and fluxes) and relevant process parameters. CARDAMOM explores a parameter hyper-volume for a fast-running intermediate-complexity model, DALEC (Data Assimilation Linked Ecosystem Carbon), and accepts parameter sets that generate model outputs consistent with observations and their uncertainty. Data used as inputs include time series information on leaf area index (LAI) magnitude and uncertainty that is extracted from the $1\,\mathrm{km} \times 1\,\mathrm{km}$ 8 d product from Copernicus Service Information (2020; Baret et al., 2016). Fire and forest biomass removal was imposed using earth observation information. The MODIS burned fraction product (Giglio et al., 2018) determines the areas where fire is imposed. Emissions are determined by assuming the product of the MODIS burned fraction input, the simulated biomass pools (labile, foliage, roots, wood, litter and soil) and tissue-specific combustion completeness (CC) parameters. The CC parameters are estimated on a per-pixel basis as

part of the CARDAMOM process. As part of DALEC's fire model, a fraction of the burned but not combusted biomass pools undergoes mortality (tissue resilience), resulting in the generation of litter. For details see Exbrayat et al. (2018). Forest biomass removal is imposed using the Global Forest Watch (GFW) forest cover loss product (Hansen et al., 2013). Meteorological drivers are drawn from the Climatic Research Unit and Japanese reanalysis (CRU-JRA) v1.1 dataset, a 6-hourly $0.5° \times 0.5°$ reanalysis (University of East Anglia Climatic Research Unit and Harris, 2019). For more details see Smallman et al. (2021).

2.2.3 Estimation of carbon emissions from fires

To estimate the contribution of biomass burning emissions to total carbon emissions from Amazonia, we estimated fire emissions with an independent inversion with TOMCAT/INVICAT by assimilating total column carbon monoxide (CO) values from MOPITT radiometer data (V8) on the Terra satellite (Deeter et al., 2019) globally. Note that in this inversion no vertical profile data for the Amazon region were assimilated. Recent studies by Zheng et al. (2019) and Naus et al. (2022) have shown that this approach for deriving fire emissions is complementary to surface remote-sensing-based methods. Due to the high density of available observational data, we carried out this inversion at $2.8° \times 2.8°$ horizontal resolution with 60 vertical levels up to 0.1 hPa. We used uncorrelated prior grid cell emission uncertainties of 450 % to give a global annual uncertainty of 15 %. The model was sampled at the longitude and latitude of each MOPITT retrieval, and the corresponding averaging kernels were applied to produce a model total column comparable to that of the satellite. For use in the inversion, we took an error-weighted average hourly mean of all retrievals within each grid cell and applied to these uncorrelated observation uncertainties of 20 % of the observed total column value added in quadrature to the supplied uncertainties. Averaging the observations within each grid cell reduces the need to apply observational error correlations. As prior fluxes we use fire emissions from GFED V4.1s (van der Werf et al., 2017), anthropogenic and oceanic emissions from CMIP6 (Hoesly et al., 2018), and direct biogenic emissions from CCMI (Chemistry–Climate Model Initiative; Morgenstern et al., 2017), as the secondary formation from isoprene, assumed to be instantaneous, is applied as a surface flux. For secondary formation from methane, monthly mean methane concentrations were taken from a previous TOMCAT-based methane inversion where the reaction with OH led directly to CO (Wilson et al., 2021).

To estimate CO flux from fire, we remove the non-fire CO fluxes from the total CO flux we estimated by multiplying the CO flux by the prior fire fraction of the total flux in that grid cell. This means that it is not possible to produce posterior fire emissions in cells which contain no prior fire emissions. Finally, we convert the CO fluxes to carbon fluxes by multiplying the CO fluxes with a biomass burning emission ratio of 16 $(\text{ppm}\,CO_2)\,/\,(\text{ppm}\,CO)$, based on the mean $CO:CO_2$ ratio of four Amazon sites estimated by vertical profile measurements by Gatti et al. (2021a). Note that these fire CO_2 emissions were not used as a fixed prior in the CO_2 inversion: instead, we subtracted these from the terrestrial non-fossil CO_2 flux estimated in the inversion to derive net biome exchange (NBE) of the biosphere.

To evaluate our carbon fire emission estimate, we compare our CO_2 fire flux and NBE flux from our CO TOMCAT-based inversion with CO_2 fire flux estimates based on CO inversion estimates from Naus et al. (2022). For the comparison, we used their posterior Amazon biomass burning inversion estimates based on the CAMS Global Fire Assimilation System (GFAS v1.2, Kaiser et al., 2012) as a prior, with the optimized CO emissions assimilating MOPITT data for the South American domain (for detailed information about the inversions see Naus et al., 2022). The TM5 model used for these inversions used a nested grid over the Amazon region with a horizontal resolution of $1° \times 1°$ and 25 vertical levels. Fluxes were optimized on a 3 d basis, and fire emissions were emitted using vertical distributions from a fire emission model. It should be noted that NBE fluxes calculated based on TOMCAT total carbon fluxes and TM5 fire emissions might have large errors due to the many differences between the methodologies and transport schemes in the two models. We estimated NBE fluxes by subtracting these CO_2 from fires from the total CO_2 flux estimated in our inversion. Note that CO_2 fire flux estimates based on Naus et al. (2022) inversions were done using $CO:CO_2$ ratios based on GFAS emission factors for each grid cell. Considering that estimates from Naus et al. (2022) were done between April and December and for a different Amazon area, for comparison we recalculated our CO_2 and CO TOMCAT-based inversions to the same area and time period (April–December over the 9 years).

2.2.4 Cumulative water deficit (CWD)

As an indicator of plant soil water stress we use climatic cumulated water deficit (CWD). CWD is a monthly soil water balance based on two simplifying assumptions: 0.1 m per month evapotranspiration and that any excess water runs off. Thus,

$$\mathrm{CWD}_{i,j}(t) = \begin{cases} 0 & \text{if } \mathrm{CWD}_{i,j}(t-1) + \mathrm{Precip}(t) - 0.1\,(\text{m per month}) > 0 \\ \mathrm{CWD}_{i,j}(t-1) + \mathrm{Precip}(t) - 0.1\,(\text{m per month}) & \text{else,} \end{cases} \quad (1)$$

where t is time (month), and i and j are grid cell indices. Furthermore, assuming that soil is fully recharged during the wettest month, CWD is reset to zero at the month of maximum precipitation, calculated separately for each grid cell as a climatic mean. From the monthly CWD maps, "maximum climatic water deficit" is defined as the maximum over the 11-month period following the month with maximum precipitation. We use precipitation estimates provided by TRMM

(version 7) (Tropical Rainfall Measuring Mission; Huffman et al., 2001), which has a $0.25° \times 0.25°$ latitude by longitude spatial resolution.

2.2.5 Temperature

For temperature analysis we used 2 m air temperatures from ERA-5 that are the monthly means of daily means since 1959 (here used between 2010 and 2018) and with a resolution of $0.25° \times 0.25°$ latitude–longitude, obtained from the ECMWF (https://doi.org/10.24381/cds.f17050d7; Hersbach et al., 2023, 2020).

2.2.6 Solar radiation

For solar radiation we used the global monthly mean surface shortwave solar radiation downward flux under all-sky conditions, between 2010 and 2018, obtained from the Clouds and the Earth's Radiant Energy System (CERES-EBAF Ed4.1; https://ceres-tool.larc.nasa.gov/ord-tool/jsp/EBAF42Selection.jsp, last access: 26 July 2022) at 1° resolution (Loeb et al., 2018; Kato et al., 2018).

2.2.7 Burned area

Burned area data were obtained from the Moderate Resolution Imaging Spectroradiometer (MODIS) Collection 6 MCD64A1 burned area product (Giglio et al., 2018). This collection provides monthly tiles of burned area with 500 m spatial resolution over the globe and was resampled to $1° \times 1°$ spatial resolution. The algorithm to estimate burned area uses several parameters from the Terra and Aqua satellite products, including daily active fire (MOD14A1 and Aqua MYD14A1), daily surface reflectance (MOD09GHK and MYD09GHK), and annual land cover (MCD12Q1) (Vermote et al., 2002; Justice et al., 2002; Friedl et al., 2010).

3 Results

3.1 Spatial distribution and seasonal pattern of Amazon carbon fluxes

To evaluate how well the inversion fitted the assimilated Amazon vertical profile data we compared the prior and posterior mole fractions with the observations (Fig. 2) for the mean observations from Amazon vertical profiles both below 1.5 km and above 3.5 km altitude. Estimated a posteriori CO_2 mole fractions have a similar magnitude and positive trend to the observations including the global posterior global mean mole fraction which follows the global trend (Fig. A1). In our Amazon mole fractions we observed a large improvement after the assimilation of observations in the model: the mean difference between estimated mole fraction and observations was reduced by 57 % and 49 % for the mean mole fractions below 1.5 km and above 3.5 km altitude, respectively (Fig. 2 and Table A2). In addition to a decrease in residuals, we also found higher correlations between the observations and the posterior mole fraction compared to the difference between observations and prior mole fractions (Fig. 2).

In Fig. 3 we display the 2010–2018 quarterly and annual mean prior total, posterior total, and posterior fire carbon flux distributions in the Amazon region to show the long-term flux distribution over this period. The 9-year mean prior flux distribution shows a source of carbon to the atmosphere during the first quarter of the year (January–March) in the western-central region, while it shows a sink of carbon between July and December, mainly occurring between July and September, i.e., during the dry season. After assimilating the Amazon vertical profile data, the posterior fluxes had a different seasonal pattern, with a significant sink in the central Amazon during January and March and a source to the atmosphere in the western region. In addition, a carbon source to the atmosphere was estimated in the eastern Amazon from July to September, which is consistent with the 9-year mean carbon emissions from fires estimated in this region over this time based on the CO inversions using MOPITT data and with the drought period in the Amazon region (Fig. 3c and d).

Our data reveal distinct spatial and seasonal carbon flux patterns in the 9-year monthly means and a significant change in posterior fluxes when vertical profile data were assimilated in the model (linear regression between posterior flux with Amazon data and prior flux: $r = 0.13$ and $p = 0.16$). Posterior total fluxes obtained without assimilating the Amazon vertical profile data result in a similar seasonal pattern as the prior total flux (linear regression between posterior flux without Amazon data and prior flux: $r = 0.66$ and $p < 0.05$), mainly between January and March, showing the Amazon as a source of carbon to the atmosphere (Fig. A2). This is in contrast with the posterior total flux estimates when the Amazon vertical profile data are assimilated in the inversions. The posterior total flux without the Amazon vertical profile data also shows an uptake of carbon during May and June similar to the prior total fluxes but with a reduction in the magnitude of these fluxes, particularly in the eastern Amazon (Figs. 3 and 4). These results indicate the strong influence and thus importance of Amazonian regional data in the inversions on constraining the Amazon carbon flux estimates, as is also found by van der Laan-Luijkx et al. (2015) and Botía Bocanegra (2022).

Large carbon emissions from fires were observed in Amazonia from August to December, mainly from the south and east regions (Figs. 3, 4 and 5). Fires also contribute emissions to the atmosphere between January and March but mainly from the western-central region due to fires occurring in the Northern Hemisphere (Figs. 3, 4 and 5).

To estimate the CO_2 net biome exchange (NBE) we subtracted the fire emissions calculated using the estimated CO fluxes by TOMCAT inverse modeling (Fig. A3) from our posterior total fluxes (Figs. 4, 5, A4 and A5). Our NBE represents the balance between photosynthesis and respiration. We

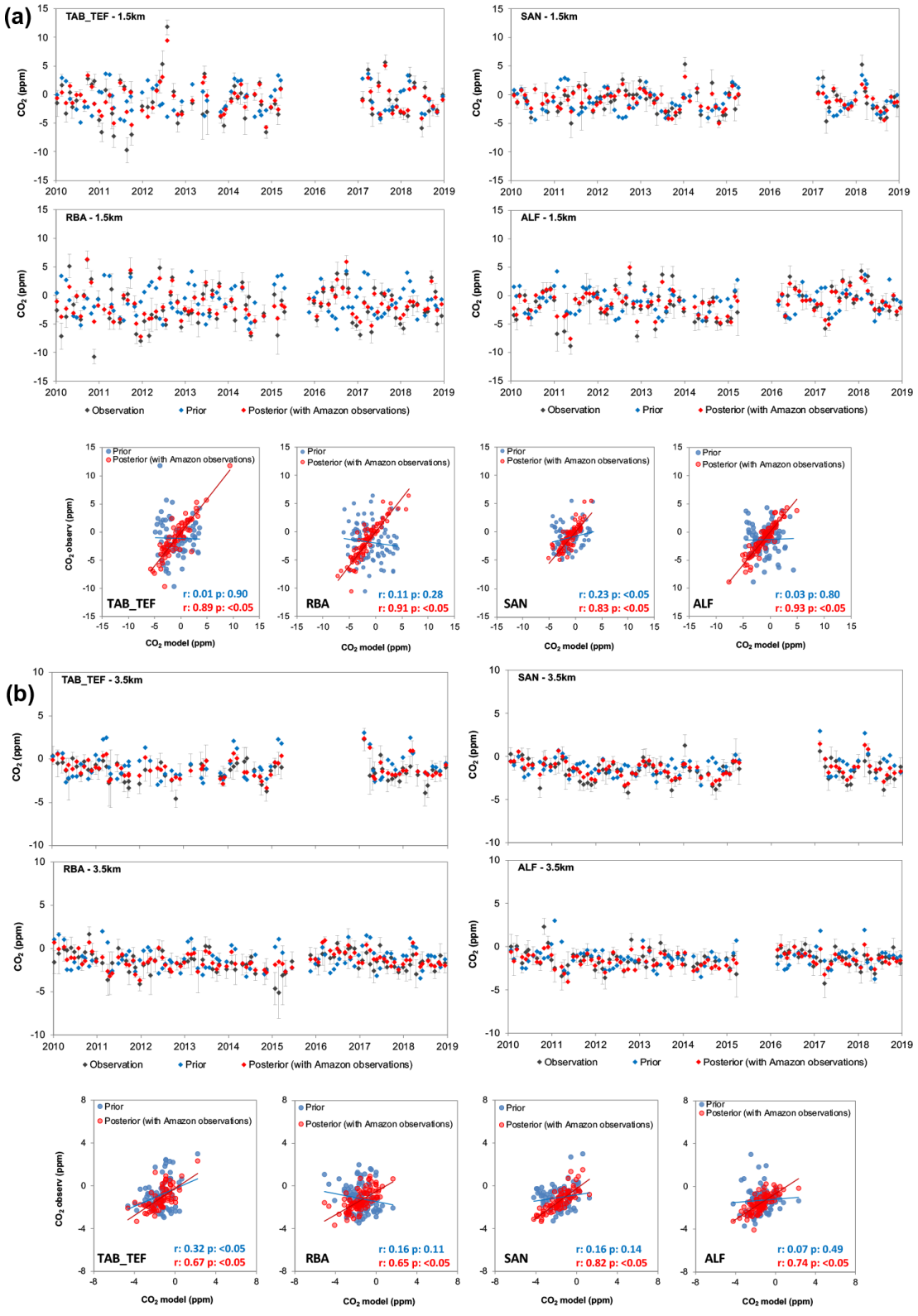

Figure 2. Detrended monthly mean CO_2 mole fractions (ppm) for prior (with CASA as land–biosphere prior flux), posterior and Amazon vertical profiles and its linear regressions, where panel **(a)** is the mean below 1.5 km altitude (planetary boundary layer levels and **(b)** the mean above 3.5 km altitude (vertical profile free troposphere) for each of the vertical profile sites. The model results were extracted for the grid cell where each site is located. After detrending, we subtracted the global mean mole fraction from the observation and model mole fractions. Error bars represent the observation uncertainties.

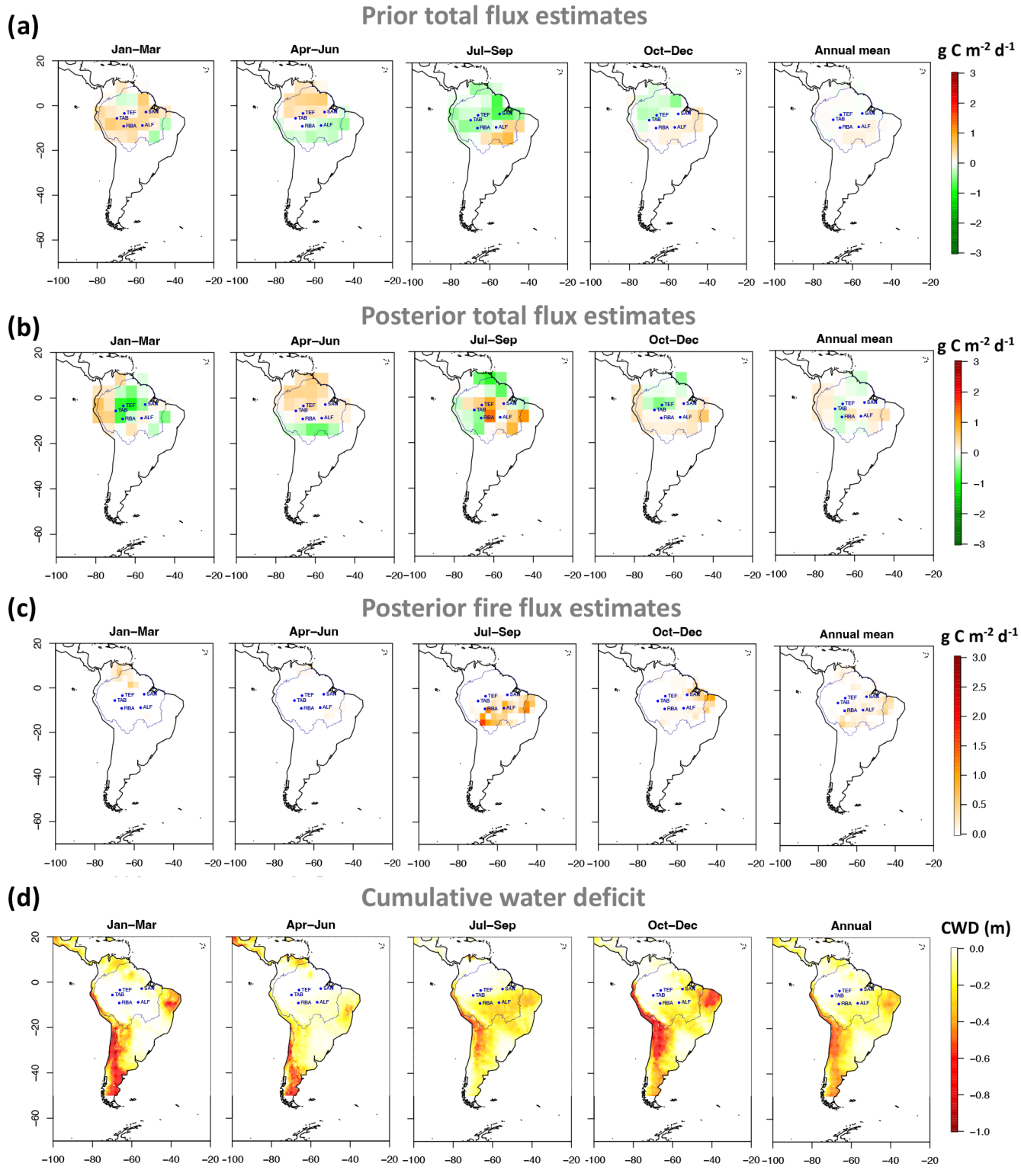

Figure 3. Quarterly and annual mean **(a)** prior total (with CASA as land–biosphere prior flux); **(b)** posterior total; **(c)** posterior fire carbon fluxes, where a positive value indicates a net emission of C while a negative value indicates a net uptake; and **(d)** cumulative water deficit (CWD) for the Amazon region between 2010 and 2018. The blue contour represents the Amazon area, based on Eva and Huber (2005).

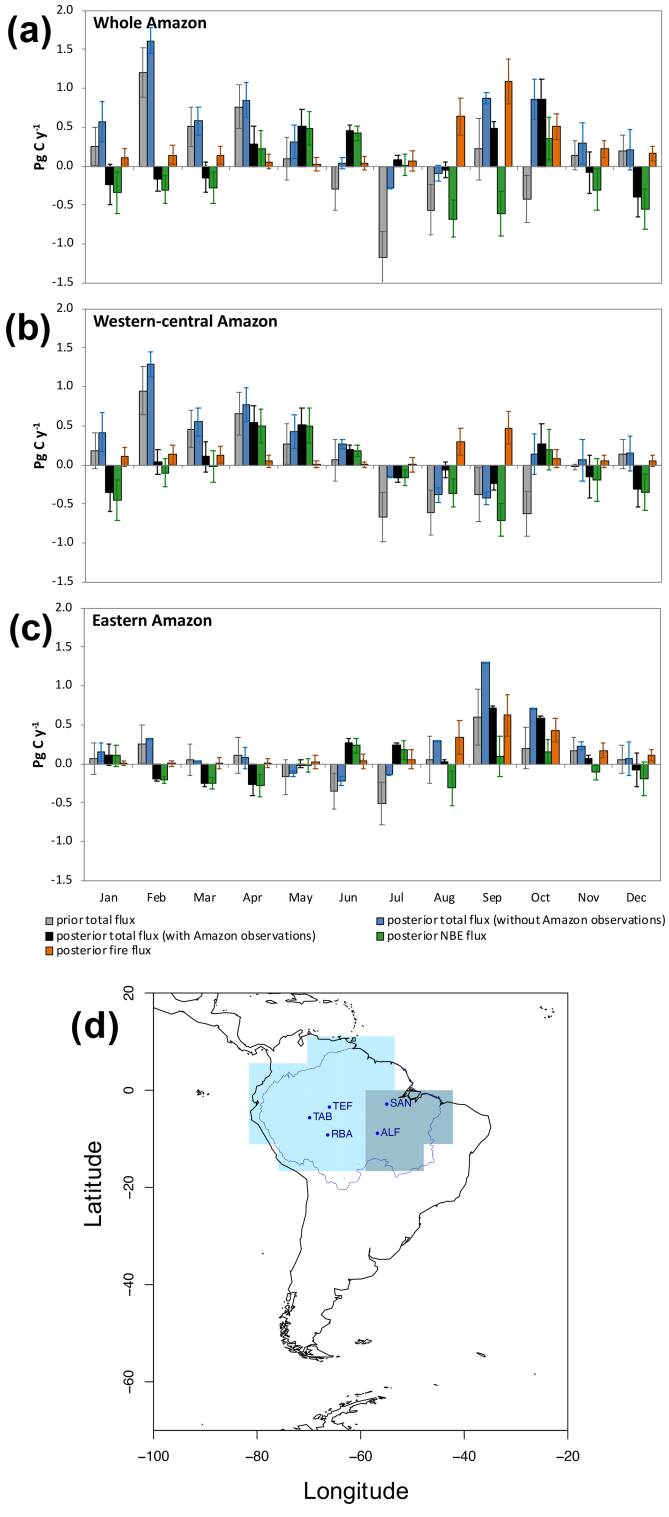

Figure 4. The 9-year monthly mean (2010–2018) carbon fluxes for the **(a)** whole Amazon, **(b)** western-central Amazon and **(c)** eastern Amazon areas: prior total flux (grey bars), posterior total flux without the Amazon vertical profile observations in the inversion (blue bars), posterior total flux with the Amazon vertical profile observations in the inversion (black bars), posterior fire fluxes using MOPITT carbon monoxide observations in the inversion (orange bars) and posterior NBE fluxes, which are the result of the subtraction of the posterior fire fluxes from the posterior total fluxes of the Amazon vertical profile observations in the inversion (green bars), representing the net biome exchange. The error bars represent the monthly mean uncertainties. **(d)** The Amazon mask used in the study; the whole Amazon area is the sum of western-central Amazon and eastern Amazon areas. The blue contour represents the Amazon area, based on Eva and Huber (2005).

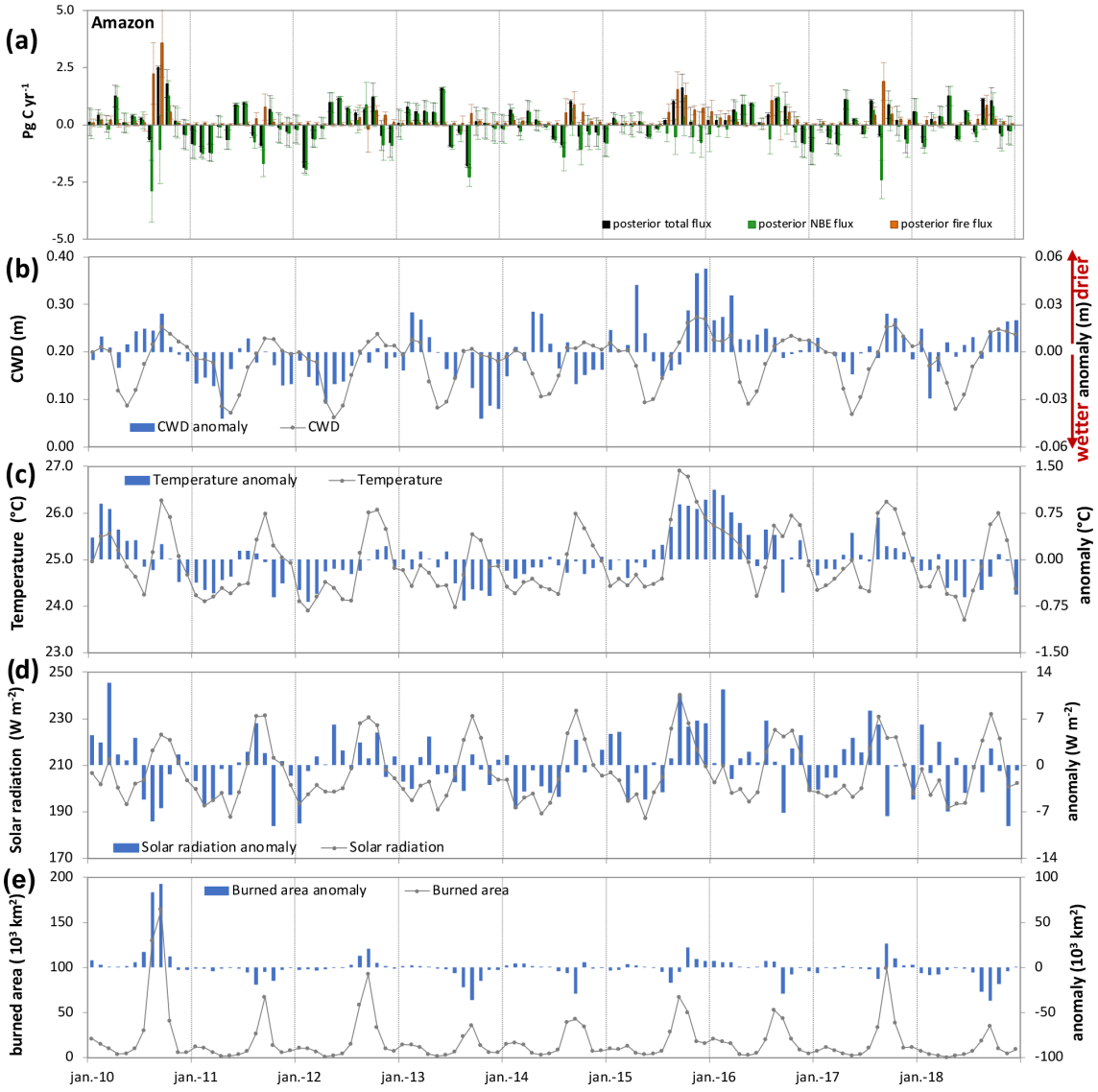

Figure 5. **(a)** Monthly mean carbon fluxes for the whole Amazon area: posterior total flux with the Amazon vertical profile observations in the inversion (black bars), posterior fire fluxes using MOPITT carbon monoxide observations in the inversion (orange bars) and posterior NBE fluxes which are the result of the subtraction of the posterior fire fluxes from the posterior total fluxes with the Amazon vertical profile observations in the inversion (green bars), representing the net biome exchange. Monthly mean and anomalies of **(b)** cumulative water deficit (CWD), **(c)** temperature, **(d)** shortwave solar radiation downward flux (all sky) and **(e)** burned area for the Amazon area.

use the following sign convention: positive NBE is a flux to the atmosphere. According to our results, the forest, not considering fire emissions, is a sink during the wet season and still acts as a sink in part of the dry season, except in July and October (Figs. 3 and 4). This dry season sink compensates for part of the carbon emissions from fires but with the sink located mainly in the western-central Amazon (Fig. 3). During the years with strong droughts such as 2010 and 2015–2016, a reduction in this dry season uptake (near neutrality) was estimated (Figs. 4, A4 and A5, discussed in detail in Sect. 4). In the western-central region we estimate a positive NBE flux to the atmosphere between April and June, which could be caused by emissions from decomposition processes (Figs. 4 and A4), as the carbon emissions due to dead wood decay in the years following a burning event (Silva et al., 2020; Anderson et al., 2015). This result resembles the seasonal cycle of NBE found by Botía et al. (2022), who used Amazon Tall Tower Observatory (ATTO) CO_2 time series data to find NBE rapidly declining at the end of the wet season, resulting in a source of CO_2 in June. In the eastern region we also estimate positive NBE fluxes (during June and July) that could be related to the decomposition process, but these emissions have a lower magnitude than those observed in the western-central region. We highlight that the southern border

of the Amazon region is characterized by a steady transition from the Amazon lowland rainforest to a mainly non-forested landscape, with predominately open vegetation types, such as savannas (campos cerrados and alluvial flooded savannas), savanna woodlands (cerradão) and other scrubby vegetation types (Eva and Huber, 2005). It also includes deforested areas with land use change conversion (Fig. A6).

We also investigated the possible relation of climate conditions with the intra-annual variability in total CO_2 fluxes. An increase in the net carbon loss to the atmosphere was observed during warmer ($r = 0.34$, and Student's t test $p < 0.05$) and drier ($r = 0.61$, $p < 0.05$) periods, during which solar radiation ($r = 0.20$, $p < 0.05$) and burned area ($r = 0.22$, $p < 0.05$) also increased. Linear regressions between posterior monthly mean fire fluxes and temperature, CWD, solar radiation and burned area all reveal significant correlations ($r = 0.61$, $p < 0.05$; $r = 0.33$, $p < 0.05$; $r = 0.52$, $p < 0.05$; and $r = 0.86$, $p < 0.05$, respectively) (Figs. A7 and A8). Furthermore, an increase in total and fire emissions was estimated during the strong drought years (2010 and 2015–2016) as expected. Note that the inter-annual variability in posterior CO_2 total fluxes is driven by the Amazon aircraft observations alone, as the land–biosphere prior flux is climatological (i.e., the same for every year) over the period.

No significant relationships between monthly posterior NBE fluxes and climate variables were observed (Fig. A9). We also investigated the correlation between NBE fluxes and climate variables with a time lag (1, 2 and 3 months of lag), but no significant correlation was observed. For western-central and eastern Amazon regions we found a similar relation between posterior fire fluxes and climate conditions as what was observed for the Amazon as a whole (Figs. A4, A5 and A8).

3.2 Amazon carbon balance and its inter-annual variability

When the data from the aircraft vertical profiles were assimilated in the inversions, the posterior total flux estimates over the period from 2010 to 2018 (including fire emissions) of $0.13 \pm 0.17\,\mathrm{Pg\,C\,yr^{-1}}$ are positive, with the majority of the emissions coming from the eastern region ($0.10 \pm 0.08\,\mathrm{Pg\,C\,yr^{-1}}$; Table 1). A larger emission to the atmosphere was estimated by the inversions when only NOAA surface site data were assimilated (without the data from the Amazon vertical profiles), resulting in a total emission of $0.48 \pm 0.17\,\mathrm{Pg\,C\,yr^{-1}}$ (including fire emissions). Fire emissions are the main reason for the flux to the atmosphere over the period ($0.26 \pm 0.13\,\mathrm{Pg\,C\,yr^{-1}}$), with the largest contribution also coming from the eastern region (Table 1). Part of these fire emissions are compensated for by the forest uptake in both the western-central and eastern Amazon regions (72 % and 33 % of the fire emissions, respectively). We highlight that the Amazon region is a carbon source to the atmosphere when we include fire emissions over this period, with an uptake by the forest (NBE flux) that compensates for 50 % of the fire emissions.

Linear regressions between annual mean posterior total flux and temperature, CWD, solar radiation and burned area yield significant correlations: $r = 0.55$, $p = 0.12$; $r = 0.62$, $p = 0.07$; $r = 0.54$, $p = 0.13$; and $r = 0.50$, $p = 0.17$, respectively. These annual mean correlations are driven mainly by the drought years 2010 and 2015–2016. In addition, we found similar relationships between annual mean posterior fire flux and temperature, CWD, solar radiation and burned area ($r = 0.75$, $p < 0.05$; $r = 0.68$, $p < 0.05$; $r = 0.56$, $p = 0.12$; and $r = 0.84$, $p < 0.05$, respectively) (Figs. 5, A10 and A11). However, we did not find any significant relationships between annual mean posterior NBE flux and climate variables (temperature, CWD and solar radiation; Fig. A12). Note that our total emission estimates could be overestimated or underestimated during 2015 and 2016 because of the low number of vertical profile data available for this period (Fig. A13).

CO_2 flux estimates over our 9-year study period indicate that Amazonian total, NBE and fire emissions do not exhibit significant time trends for the western-central or the eastern regions (Fig. 6).

3.3 Sensitive tests

We also estimate Amazonian CO_2 fluxes using our atmospheric inversion but replacing the biosphere prior flux estimates of CASA with the estimates of CARDAMOM for the South American region (Fig. A14). We also observed a large improvement after the assimilation of observations in the model for the inversions using CASA as prior flux estimates (Fig. A15 and Table A2). Comparing both estimates (from CARDAMOM and CASA models) of land–biosphere fluxes used as prior in the inversions, we found that CARDAMOM shows a large carbon uptake (prior total flux of $-2.50 \pm 0.43\,\mathrm{Pg\,C\,yr^{-1}}$) for the Amazon region in contrast to the estimates from the CASA model (prior total flux of $0.08 \pm 0.24\,\mathrm{Pg\,C\,yr^{-1}}$). CARDAMOM prior flux estimates show a large carbon sink in the Amazon between January and March in contrast with a carbon source to the atmosphere estimated by the CASA model. The large uptake was not reproduced after the assimilation of Amazon observational data. After assimilating the Amazon vertical profile data in the inversions using CARDAMOM as the land–biosphere prior, the posterior estimate shows a strong reduction in the uptake for the Amazon region (posterior total flux of $-0.19 \pm 0.17\,\mathrm{Pg\,C\,yr^{-1}}$) compared to the prior (Fig. A14). This result shows that the large land–biosphere sink estimated by CARDAMOM is inconsistent with the Amazon atmospheric vertical profile data. Although the inversion using CARDAMOM as a prior estimates the Amazon to be a small overall carbon sink, while the inversion using the CASA model as a prior estimates the Amazon to be a small

Table 1. The 9-year mean prior total, posterior total without the vertical profile observations assimilated in the inversions, and posterior total with the vertical profile observations assimilated in the inversions and fire fluxes for the whole Amazon, west-central and east Amazon regions.

Amazon C land fluxes 2010–2018 ($Pg\,C\,yr^{-1}$)			
Region	Amazon	Western-central Amazon	East Amazon
Prior total flux	0.08 ± 0.24	0.03 ± 0.21	0.04 ± 0.20
Posterior total flux (without Amazon observations)	0.48 ± 0.17	0.26 ± 0.16	0.23 ± 0.07
Posterior total flux (with Amazon observations)	0.13 ± 0.17	0.03 ± 0.17	0.10 ± 0.08
Posterior fire flux	0.26 ± 0.13	0.11 ± 0.10	0.15 ± 0.11
Posterior NBE flux (without Amazon observations)	0.21 ± 0.20	0.12 ± 0.18	0.09 ± 0.13
Posterior NBE flux (with Amazon observations)	-0.13 ± 0.20	-0.08 ± 0.18	-0.05 ± 0.13

source to the atmosphere ($0.13 \pm 0.17\,Pg\,C\,yr^{-1}$), the intra-annual seasonality from both inversions is similar (Fig. A14). Also, both posterior estimates have a similar spatial flux distribution. Posterior flux estimates using CARDAMOM as the land–biosphere prior flux also estimate the eastern Amazon to be a carbon source to the atmosphere from July to September, and during January and March to be a significant sink in the central Amazon, while the western region is estimated to be a source to the atmosphere (Fig. A14).

We compared fire fluxes based on CO inversion estimates of Naus et al. (2022) and estimated NBE fluxes, subtracting these CO_2 estimated from fires from the total CO_2 flux estimated in our inversion, with our estimates based on TOMCAT CO inversions. We found similar intra- and inter-annual variability and flux magnitudes when compared to our NBE and fire estimates based on TOMCAT CO inversions with estimates based on their CO inversions (Fig. A16 and Table A3). Both CO inversions assimilated the same MOPITT observations but differ in inversion methodology, model transport and emission factor to convert CO flux from fires to CO_2 flux. Some difference in both estimates (for both fire and NBE fluxes) could be related to these differences in both approaches. To get a truly independent estimate of NBE from another inversion model, it would need to estimate both total carbon and fire carbon. Also, both CO_2 fire emissions (based on the two different CO optimized fluxes) could be used as prior in a future CO_2 inversion to investigate the dependence of the fire estimates in the NBE optimization.

3.4 Comparison to independent observations

To validate our inversion results we used independent in situ observations of CO_2 mole fractions in the Amazon region made at the ATTO site (2.14° S, 58.99° W, measurements at 80 m height; Lavric and Walter, 2022a, b, c, d, e, f, g; Botía et al., 2022) and with vertical profile data measured at Manaus (MAN) (2.59° S, 60.21° W, with profiles extending from approximately 0.2 to 5 km height aboveground; Miller et al., 2021). For the comparison between modeled and observed mole fractions, the model data were sampled at the grid cell closest to the site locations.

The ATTO time series is based on observations made between 2012 and 2018 (Lavric and Walter, 2022a, b, c, d, e, f, g), and the data presented here are available upon request at https://attodata.org (last access: 11 May 2023). We calculate the monthly mean mole fractions based on only daytime dry-air mole fractions (13:00–17:00 LT), which were representative of well-mixed convective conditions (Botía et al., 2022). In addition, for the year 2015 we remove from the comparison the months without vertical profile data assimilated in the inversion. Although the ATTO measurements are made 80 m aboveground, i.e., quite close to the ground, in general we found good agreement between model and observations (Fig. A17), with a reduction of the bias after the inversion from 0.9 ppm (range of −3.9 to 7.7) to 0.3 ppm (range of −5.3 to 4.7) (t test: $p < 0.05$).

In addition, we compare the model mole fractions to the aircraft vertical profiles in MAN above 3.5 km and below 1.5 km (Fig. A18). The data record from MAN for the same period of our inversions is for the years 2017 and 2018. Flights are undertaken approximately every 2 weeks, and in general measurements were taken between 12:00 and 13:00 LT, when the boundary layer is fully developed. We found a reduction in the bias between model and observations after the inversions for the mean below 1.5 km from −0.3 ppm (range of −6.5 to 6.6) to 0.2 ppm (range of −4.3 to 5.0) (t test: $p = 0.17$) and for the mean above 3.5 km height from −0.1 ppm (range of −3.1 to 2.1) to −0.4 ppm (range of −1.9 to 0.5) (t test: $p = 0.13$). We also found a reduction of the mean bias of the difference between the mean below 1.5 km and the vertical profile free troposphere (above 3.5 km) from −0.2 ppm (range of −5.4 to 7.6) to 0.6 ppm (range of −4.2 to 5.6) (t test: $p = 0.08$). The posterior comparisons also show an increase in the bias close to the surface, which means that the local sources close to this site might be overestimated at this model resolution, there might be errors in the model's representation of vertical mixing or a positive bias in the assimilated Amazon vertical profiles in this

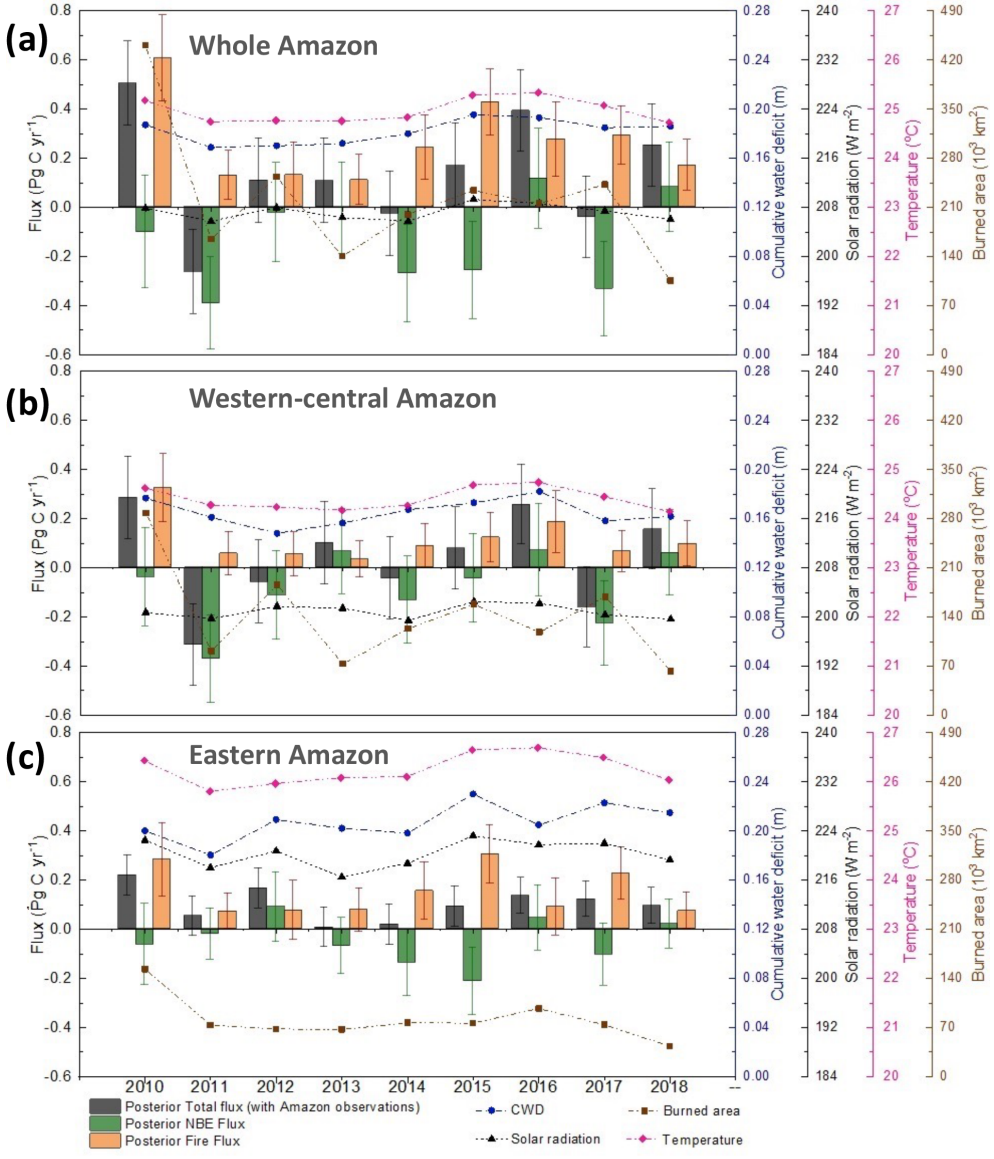

Figure 6. Annual mean carbon fluxes for the **(a)** whole Amazon, **(b)** western-central and **(c)** eastern Amazon areas: posterior total flux with the Amazon vertical profile observations in the inversion (black bars) and posterior fire fluxes using MOPITT carbon monoxide observations in the inversion (red bars). Annual cumulative water deficit (blue line), annual mean temperature (pink line), annual mean shortwave solar radiation downward flux (all sky; black line) and annual total burned area (brown line).

region may remain. However, in general the cross-validation with observations from the ATTO and MAN vertical profiles showed an improvement in the model bias and temporal variation after the assimilation of Amazon vertical profile observations.

4 Discussion

The posterior fluxes when vertical profile data were assimilated in the inversions led to a change compared to the prior in the flux seasonal cycle and additionally showed a larger reduction in the Amazon total emission in comparison with the posterior fluxes when just NOAA surface data were assimilated (Figs. 3 and 4 and Table 1). This once again highlights the importance of assimilating regional data in the inversions to better constrain the tropical forest fluxes (van der Laan-Luijkx et al., 2015; Alden et al., 2016; Botía et al., 2022). This result is not dependent on the assumed prior sources and sinks, as we also found a significant reduction of the large land–biosphere carbon uptake suggested by CARDAMOM for the Amazon region after assimilating the Amazon vertical profile data in the inversion (Fig. A14).

Using CASA model predictions as the land–biosphere prior flux, we estimate the Amazon region to be a to-

tal (i.e., including emissions from fire) net source of C of $0.13 \pm 0.17\,\mathrm{Pg\,C\,yr^{-1}}$ over our analysis period. The largest emission comes from the eastern Amazon and from the transition region between the forest and the Cerrado area (as shown in Fig. 3), while the largest uptake was observed in the western-central region. Our results indicate that the Amazon is a source of carbon to the atmosphere caused by fire emissions, which were larger than the estimated Amazon land sink, but we highlight that during this period the forest uptake removes around half of the fire emissions to the atmosphere.

Globally, the land CO_2 sink was estimated to be $3.1 \pm 0.6\,\mathrm{Pg\,C\,yr^{-1}}$ during the decade 2011–2020 (29 % of total global CO_2 emissions; Friedlingstein et al., 2022) and continued to increase during this period likely in response to increased atmospheric CO_2 (Friedlingstein et al., 2022). However, the land sink varies strongly inter-annually, with decreased land carbon uptake during El Niño events. According to Friedlingstein et al. (2022), in general the tropical region (30° S–30° N) has a carbon balance close to neutral over the 2011–2020 period; however, the tropical region is most strongly correlated with inter-annual variation of atmospheric CO_2 (Friedlingstein et al., 2022). Note that this tropical region estimate did not include the information provided by the Amazon vertical CO_2 profile data we used here. The tropics is also where the largest land use emissions occur, including the arc of deforestation in the Amazon basin (Friedlingstein et al., 2022). We did not observe an increasing trend over time in the land carbon uptake for the Amazon region, in contrast to the continued increase in the global land sink reported by Friedlingstein et al. (2022).

Based on a distributed network of 321 forest survey plots from RAINFOR, Brienen et al. (2015) estimated a 30 % decrease in the total net carbon sink into intact Amazon live biomass from $0.54\,\mathrm{Pg\,C\,yr^{-1}}$ (95 % confidence interval 0.45–0.63) in the 1990s to $0.38\,\mathrm{Pg\,C\,yr^{-1}}$ (0.28–0.49) in the 2000s. Phillips and Brienen (2017), based also on the RAINFOR network plot measurements, estimated an Amazon-wide forest biomass carbon sink between 1980 and 2010 of $0.43\,\mathrm{Pg\,C\,yr^{-1}}$ (CI 0.21–0.67). Finally, Hubau et al. (2020) reported a decrease in the Amazon net carbon sink in the last few decades from $0.68\,\mathrm{Pg\,C\,yr^{-1}}$ (CI 0.54–0.83) between 1990 and 2000 to $0.45\,\mathrm{Pg\,C\,yr^{-1}}$ (CI 0.31–0.57) between 2000 and 2010, predicting a net carbon sink of $0.25\,\mathrm{Pg\,C\,yr^{-1}}$ (CI −0.05–0.54) between 2010–2020. Our posterior NBE estimates (a sink of $0.13 \pm 0.20\,\mathrm{Pg\,C\,yr^{-1}}$) are fairly consistent with the RAINFOR results with regards to magnitude but not with the trend over time regarding observed carbon uptake, considering that the areas used for the estimates are different and that our NBE represents not only the uptake from forests but also non-fire emissions (as decomposition and degradation emissions).

Our posterior fire emissions agree with fire emission estimates for Brazilian Amazonia reported by Aragão et al. (2018), with a total fire emission of $0.21 \pm 0.23\,\mathrm{Pg\,C\,yr^{-1}}$ over the period 2003–2015, based on the relation between MOPITT CO total column and burned forest and deforestation gross CO_2 emissions data (Aragão et al., 2018). Recently, Silva et al. (2020) reported that forest fires contribute cumulative gross carbon emissions of $\sim 126\,\mathrm{Mg\,CO_2\,ha^{-1}}$ for 30 years after a fire event, with a mean annual efflux of $4.2\,\mathrm{Mg\,CO_2\,ha^{-1}\,yr^{-1}}$ and emissions from the decomposition of the dead organic matter accounting for ca. 58 % ($47.4\,\mathrm{Mg\,CO_2\,ha^{-1}}$) of total cumulated net emissions. Van der Werf et al. (2010) estimated that fires were responsible for an annual mean global carbon emission of $2.0\,\mathrm{Pg\,C\,yr^{-1}}$ (for the period 1997–2009) with significant inter-annual variability, where about 15 % ($0.29\,\mathrm{Pg\,C\,yr^{-1}}$) was associated with South American emissions mainly from the Southern Hemisphere of South America (14 %; $0.27\,\mathrm{Pg\,C\,yr^{-1}}$), according to estimates from the Global Fire Emissions Database (GFED V.3). Note that this South American emission estimate was related to a larger area than our Amazon region estimates.

We found clear intra-annual seasonality in our posterior total, fire and NBE fluxes. In general, we found over these 9 years that the Amazon is a carbon sink during November to March (wet season) and also during August and September, removing part of the fire emissions during the dry season (Figs. 4, 5, A4 and A5). Although we did not find a significant relation between our NBE seasonality and the climate variables analyzed (CWD, temperature and solar radiation), our NBE emission seasonality shows good agreement with the Amazon mean net ecosystem exchange (NEE) seasonality measured at five eddy covariance forest tower sites located in the Brazilian Amazon, Manaus forest (K34; 1999–2006), Santarém forest (K67; 2001–2005, 2008–2011 and 2015–2019), forest of Caxiuana (CAX; 1999–2003), Reserva Jarú southern forest (RJA; 2000–2002) and the seasonal inundated forest of Bananal (JAV; 2003–2006) (Gatti et al., 2021c). Our fire emission estimates showed the largest increase during the dry season months of August to October, in agreement with the increase in CWD, temperature, solar radiation and burned area (Figs. 5, A4, A5 and A8).

We found that our total and fire emission estimates' inter-annual variability correlates with climatic variations, with larger emissions occurring during hotter and drier years as in 2010 and 2015–2016. This inter-annual variability in our estimates is primarily driven by the atmospheric vertical profile data and MOPITT CO columns and not by prior estimates, as in our approach the land flux prior estimates are the same for all years. In 2010 the increase in carbon emissions was mainly caused by an increase in emissions in the western-central region, related to a large increase in fire emissions (2010 flux of $0.32 \pm 0.14\,\mathrm{Pg\,C\,yr^{-1}}$ and a 9-year mean of $0.11 \pm 0.10\,\mathrm{Pg\,C\,yr^{-1}}$; Student's t test: $p = 0.14$) and also a reduction of the uptake in relation to the 9-year mean (2010 flux of $-0.04 \pm 0.20\,\mathrm{Pg\,C\,yr^{-1}}$ and a 9-year mean of $-0.08 \pm 0.18\,\mathrm{Pg\,C\,yr^{-1}}$; $p = 0.43$). We also observed an increase in fire emissions in the eastern Amazon region during this year, but it is still lower than in the western-

central region (2010 flux of 0.28 ± 0.15 Pg C yr^{-1} and a 9-year mean of 0.15 ± 0.11 Pg C yr^{-1}; $p = 0.21$). These results are in agreement with the increase in burned areas observed in the western-central and eastern Amazon regions for the same period when compared with the 9-year mean (104 % and 89 % in western-central and eastern Amazon regions, respectively) and with an increase of 7 % in the CWD compared with the 9-year mean in the western-central region. Although some p values are larger than 0.05, these results suggest changes in the carbon cycle in 2010. High correlations between soil moisture and MOPITT-derived fire emissions were also reported by Naus et al. (2022) for the Amazonas province, confirming the important role of the moisture state of the underlying forest soils.

On the other hand, during 2016 the increase in carbon emissions was mainly related to a reduction in the forest carbon uptake in the Amazon region. Organic land carbon pools (forests, soils) were a net source to the atmosphere during this year (NBE flux of $+0.12 \pm 0.20$ Pg C yr^{-1}; Student's t test: $p = 0.14$), while fire emissions increased 61 % in the western-central Amazon in relation to the 9-year mean (2016 flux of 0.19 ± 0.13 Pg C yr^{-1} and a 9-year mean of 0.11 ± 0.10 Pg C yr^{-1}; Student's t test: $p = 0.17$). These indications of reductions in the carbon uptake could be related to hotter and drier conditions in the western-central region, with an increase of 10 % in the CWD in relation to the 9-year mean and an increase of 0.3 and 0.4 °C in the annual mean temperature in relation to the 9-year mean (the largest positive anomalies in the 9 years for both regions) in the western-central and eastern Amazon region. Recently, Fancourt et al. (2022) reported that background climate and soil conditions had a greater influence than the climatic anomalies on Amazon forest photosynthesis spatio-temporal variations but with the northwestern forests being the most sensitive to precipitation anomalies during the 2015–2016 El Niño period.

Gloor et al. (2018) reported a net flux anomaly from the Amazon of 0.5 ± 0.3 Pg C during the 2015–2016 El Niño event (between September 2015 and June 2016), based on previous inversions using TOMCAT and assimilating the Amazon vertical profile data. Our posterior total estimates showed a net flux anomaly for this period of 0.58 ± 0.20 Pg C for the whole Amazon, with 0.32 ± 0.19 and 0.26 ± 0.09 Pg C for the western-central and eastern Amazon, respectively. The majority of the anomalies observed come from a reduction in the carbon sink making NBE fluxes positive in the western-central Amazon, with a total net emission of 0.09 ± 0.22 Pg C yr^{-1} (while the 9-year means for this period show an uptake of 0.04 ± 0.15 Pg C yr^{-1}; $p = 0.25$) acting as a net carbon source to the atmosphere during this period, in addition to an increase in fire emissions at both the western-central (flux of 0.23 ± 0.14 Pg C yr^{-1} for this period with a 9-year mean of 0.11 ± 0.10 Pg C yr^{-1}; $p = 0.07$) and eastern regions (flux of 0.33 ± 0.14 Pg C yr^{-1} for this period with a 9-year mean of 0.14 ± 0.10 Pg C yr^{-1}; $p = 0.13$). Koren et al. (2018) and van Schaik et al. (2018) suggested a reduction in gross primary production, resulting from combined heat and soil moisture stress, to be a dominant mechanism in agreement with the results in Gloor et al. (2018) based on solar-induced fluorescence data measured from space.

While agricultural and deforestation fires are more closely associated with human actions than with climate (Anderson et al., 2018), forest fires are associated with a combination of human activities which provide the ignition source and climatic factors creating dry conditions (Berenguer et al., 2021). During strong drought conditions, such as the drought of 1997–1998, fires could escape from agricultural fields and burn standing primary forests that were once considered impenetrable to fire (Brando et al., 2020). A warming trend is being observed in Amazonia, evident since 1980, and it has been enhanced since 2000, a period where strong droughts occurred in 2005, 2010 and 2015–2016 (the increases in temperature vary with the dataset, time period and spatial scale of the analysis) (Marengo et al., 2021). Also, warming was observed in the eastern Amazon, and especially southeastern Amazon, at a rate almost twice as high as the western Amazon (Marengo et al., 2021). Our CWD analysis for Amazonia shows a weak drying trend for almost all regions between 1998 and 2019 (Fig. A19). The observed climate tendencies in Amazonia can be different in the western and eastern regions, and the projected changes suggest a drier and warmer climate in the east, while in the west rainfall is expected to increase in the form of more intense rainfall events (Marengo et al., 2021).

The increase in climate variability impacts both the Amazonian forest (Anderson et al., 2018) and savannah biomes, increasing tree mortality (Aragão et al., 2018) and ecosystem vulnerability to fire (Anderson et al., 2018; Silva Junior et al., 2019). The increased variability, in combination with deforestation, has changed the forest's resilience to fires, in particular in the southern Amazon, where remaining forests have become drier and thus vulnerable to wildfires during recent droughts (Brando et al., 2020). Our posterior fire estimates showed the largest emissions in the eastern Amazon region, with an increase in emissions during strong drought years, but we did not find a significant trend over the 2010 to 2018 period. The eastern Amazon is more disturbed by human activity than the western-central region, with larger deforested areas also converted to agriculture and grassy areas (Fig. A6).

The clear seasonality in our posterior total, fire and NBE fluxes is generally in agreement with that reported by Gatti et al. (2021a), based on a mass balance technique for the Amazon region as a whole and also for western and eastern regions (Fig. A20). It is important to highlight that we use a larger Amazon area in comparison with Gatti et al. (2021a). Here we included a transition region between the Amazon forest and Cerrado biomes in the southeast of Amazonia (Fig. A6). For the eastern Amazon, the seasonality of the

NBE estimate of the two approaches is more similar than the seasonality of the fire emissions. Gatti et al. (2021a) estimated fire emissions to occur during January to March, mainly in the northeastern region, while we did not estimate fire emissions during this period. Part of this difference could be related to the different regions considered as eastern Amazonia in the two studies. The region of influence of fluxes influencing CO_2 measured at the vertical profiling site (ALF and SAN sites) reported by Gatti et al. (2021a), estimated using quarterly mean back-trajectories, has contributions from the Northern Hemisphere Amazon during this time, an area not considered in our eastern Amazon region definition. The difference could also be related to the burned area fraction from the prior flux (from GFED V4.1s), which we multiplied with the CO total flux in each grid cell to derive the CO fire emissions in our inversion; the absence of burned area fractions will result in no fire emissions in the area, consequently underestimating carbon emissions caused by fire in this region. On the other hand, fire emissions during this period are observed in both approaches in the western-central region. The main difference observed in the estimates for this region was in the NBE during the dry season months of August and September, where our posterior estimates showed an uptake while the mass balance technique estimates (Gatti et al., 2021a) showed a source to the atmosphere (Fig. A20). A substantial dry season sink in the western Amazon was independently derived from ATTO CO_2 observations by Botía et al. (2022), supporting our findings here.

No significant trend over time (between 2010 and 2018) was observed in our posterior emissions, in contrast with the trend in NBE fluxes for the east Amazon region, with an increase in emissions over this time reported by Gatti et al. (2021a). Our results indicate that Amazonia is a source of carbon to the atmosphere because of fire emissions, corroborating the findings of Gatti et al. (2021a). Our 9-year mean total posterior emissions for the Amazon region are 33 % smaller than their total emission estimates, with the largest difference being observed in the eastern region (Fig. 7). The largest differences are mainly related to the fire emission estimates, while our posterior NBE estimate represents 90 % of their estimates. However, considering the range of both Amazon flux estimates, we find similar emissions (Fig. 7).

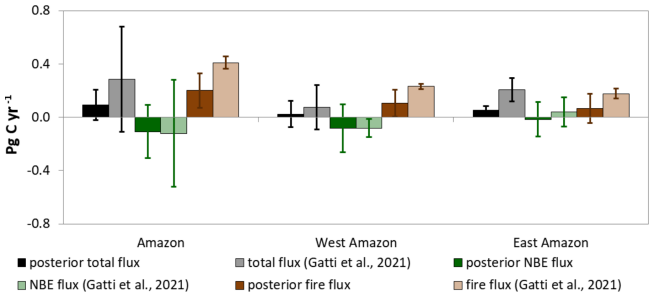

Figure 7. Comparison of the 9-year mean of carbon fluxes from the inverse modeling (prior total flux, posterior total flux, posterior NBE flux (total minus fire emissions) and posterior fire flux) and flux estimates (total, NBE and fire) using a mass balance technique in Gatti et al. (2021a). All fluxes are estimated using the Amazon areas (km^2) from Gatti et al. (2021a).

5 Conclusions

Our global inverse model estimates of CO_2 emissions using Amazon atmospheric vertical profiles and surface observations have allowed us to estimate that over the 9 years of 2010–2018 the Amazon region acted as a small carbon source to the atmosphere, with a total emission of $0.13 \pm 0.17\,\mathrm{Pg\,C\,yr^{-1}}$. The emissions were greater in eastern Amazonia ($0.10 \pm 0.08\,\mathrm{Pg\,C\,yr^{-1}}$) than in the western region, mostly because of larger fire emissions. The forest uptake (NBE) compensated for approximately 50 % of the fire emissions and was larger in the western-central region than in the eastern Amazon region (72 % and 33 % of the fire emissions, respectively). This highlights the importance of public policies to prevent deforestation and fire occurrences to reduce Amazon carbon emissions to the atmosphere and help to mitigate the effects of climate change.

Our estimated carbon fluxes were larger during the extreme drought years such as 2010, 2015 and 2016, mainly because of an increase in fire emissions and a reduction in carbon uptake. However, we did not find any significant trend in carbon emissions over the period of 2010–2018. Our analysis thus cannot provide clear evidence for a weakening of the carbon uptake by Amazonian tropical forests.

The inter- and intra-annual seasonality of the results from our inversion is in agreement with previous studies (e.g., Gatti et al., 2021a; Botía et al., 2022; Naus et al., 2022). Our study shows the benefit of using regional vertical CO_2 profile data over land to better constrain carbon emissions in tropical forests such as the Amazon, thereby improving the estimated magnitude and intra-annual seasonality of the emissions. In turn, this helps to improve global estimates and understand possible climate and human disturbance feedbacks in the carbon cycle.

Appendix A

Table A1. NOAA monitoring sites with CO_2 observation data used in the inverse model.

Code	Name	Latitude	Longitude	Time period
ALT	Alert, Nunavut, Canada	82.45° N	62.50° W	2010–2018
AMY	Anmyeon-do, Republic of Korea	36.53° N	126.32° E	2013–2018
ASC	Ascension Island, United Kingdom	7.96° S	14.40° W	2010–2018
ASK	Assekrem, Algeria	23.26° N	5.63° E	2010–2018
AZR	Terceira Island, Azores, Portugal	38.76° N	27.37° W	2010–2018
BAL	Baltic Sea, Poland	55.35° N	17.22° E	2010–2011
BHD	Baring Head Station, New Zealand	41.40° S	174.87° E	2010–2018
BKT	Bukit Kototabang, Indonesia	0.20° S	100.31° E	2010–2018
BMW	Tudor Hill, Bermuda, United Kingdom	32.26° N	64.87° W	2010–2018
BRW	Barrow Atmospheric Baseline Observatory, United States	71.32° N	156.61° W	2010–2018
CBA	Cold Bay, Alaska, United States	55.21° N	162.72° W	2010–2018
CGO	Cape Grim, Tasmania, Australia	40.68° S	144.69° E	2010–2018
CHR	Christmas Island, Republic of Kiribati	1.70° N	157.15° W	2010–2018
CIB	Centro de Investigacion de la Baja Atmosfera (CIBA), Spain	41.81° N	4.93° W	2010–2018
CPT	Cape Point, South Africa	34.35° S	18.48° E	2012–2018
CRZ	Crozet Islands, France	46.43° S	51.84° E	2010–2018
DRP	Drake Passage	59.00° S	64.69° W	2010–2018
DSI	Dongsha Island, Taiwan	20.69° N	116.72° E	2010–2018
EIC	Easter Island, Chile	27.15° S	109.42° W	2010–2018
GMI	Mariana Islands, Guam	13.38° N	144.65° E	2010–2018
HBA	Halley Station, Antarctica, United Kingdom	75.605° S	26.21° W	2010–2018
HPB	Hohenpeissenberg, Germany	47.80° N	11.02° E	2010–2018
HSU	Humboldt State University, United States	41.05° N	124.75° W	2010–2017
HUN	Hegyhátsál, Hungary	46.95° N	16.65° W	2010–2018
ICE	Stórhöfði, Vestmannaeyjar, Iceland	63.39° N	20.28° W	2016–2018
IZO	Izana, Tenerife, Canary Islands, Spain	28.30° N	16.49° W	2010–2018
KEY	Key Biscayne, Florida, United States	25.66° N	80.15° W	2010–2018
KUM	Cape Kumukahi, Hawaii, United States	19.73° N	155.01° W	2010–2018
LLB	Lac La Biche, Alberta, Canada	54.95° N	112.46° W	2010–2013
LLN	Lulin, Taiwan	23.47° N	120.87° E	2010–2018
LMP	Lampedusa, Italy	35.51° N	12.63° E	2010–2018
MEX	High Altitude Global Climate Observation Center, Mexico	18.98° N	97.31° W	2010–2018
MHD	Mace Head, County Galway, Ireland	53.32° N	9.89° W	2010–2018
MID	Sand Island, Midway, United States	28.21° N	177.38° W	2010–2018
MLO	Mauna Loa, Hawaii, United States	19.53° N	155.57° W	2010–2018
NAT	Farol De Mãe Luiza Lighthouse, Brazil	5.79° S	35.18° W	2010–2018
NMB	Gobabeb, Namibia	23.58° S	15.03° E	2010–2018
NWR	Niwot Ridge, Colorado, United States	40.05° N	105.58° W	2010–2018
OXK	Ochsenkopf, Germany	50.03° N	11.80° E	2010–2018
PAL	Pallas-Sammaltunturi, GAW Station, Finland	67.97° N	24.11° E	2010–2018
POC000	Pacific Ocean (0° N)	0.00°	–	2010–2017
POCN05	Pacific Ocean (5° N)	5.00° N	–	2010–2017
POCN10	Pacific Ocean (10° N)	10.00° N	–	2010–2017
POCN15	Pacific Ocean (15° N)	15.00° N	–	2010–2017
POCN20	Pacific Ocean (20° N)	20.00° N	–	2010–2017
POCN25	Pacific Ocean (25° N)	25.00° N	–	2010–2017
POCN30	Pacific Ocean (30° N)	30.00° N	–	2010–2017
POCS05	Pacific Ocean (5° S)	5.00° S	–	2010–2017
POCS10	Pacific Ocean (10° S)	10.00° S	–	2010–2017
POCS15	Pacific Ocean (15° S)	15.00° S	–	2010–2017
POCS20	Pacific Ocean (20° S)	20.00° S	–	2010–2017

Table A1. Continued.

Code	Name	Latitude	Longitude	Time period
POCS25	Pacific Ocean (25° S)	25.00° S	–	2010–2017
POCS30	Pacific Ocean (30° S)	30.00° S	–	2010–2017
PSA	Palmer Station, Antarctica, United States	64.77° S	64.05° W	2010–2018
PTA	Point Arena, California, United States	38.95° N	123.74° W	2010–2011
RPB	Ragged Point, Barbados	13.16° N	59.43° W	2010–2018
SDZ	Shangdianzi, China	40.65° N	117.11° E	2010–2015
SEY	Mahé Island, Seychelles	4.68° S	55.53° E	2010–2018
SGP	Southern Great Plains, Oklahoma, United States	36.60° N	97.48° W	2010–2018
SHM	Shemya Island, Alaska, United States	52.71° N	174.12° E	2010–2018
SMO	Tutuila, American Samoa	14.24° S	170.56° W	2010–2018
SUM	Summit, Greenland	72.59° N	38.42° W	2010–2018
SYO	Syowa Station, Antarctica, Japan	69.01° S	39.59° E	2010–2018
TAP	Tae-ahn Peninsula, Republic of Korea	36.73° N	126.13° E	2010–2018
THD	Trinidad Head, California, United States	41.05° N	124.15° W	2010–2017
TIK	Hydrometeorological Observatory of Tiksi, Russia	71.59° N	128.88° E	2011–2018
USH	Ushuaia, Argentina	54.84° S	68.31° W	2010–2018
UTA	Wendover, Utah, United States	39.90° N	113.71° W	2010–2018
UUM	Ulaan-Uul, Mongolia	44.45° N	111.09° E	2010–2018
WIS	Weizmann Institute of Science at the Arava Institute, Ketura, Israel	29.96° N	35.06° E	2010–2018
WLG	Mt. Waliguan, Peoples Republic of China	36.28° N	100.89° E	2010–2018
ZEP	Ny-Ålesund, Svalbard, Norway and Sweden	78.90° N	11.88° E	2010–2018

Table A2. Mean difference between CO_2 mole fraction model estimates and observations.

CO_2 mole fraction mean difference (ppm)				
	CASA as land–biosphere prior flux			
Site	Mean below 1.5 km altitude		Mean above 3.5 km altitude	
	Prior – observed	Posterior – observed	Prior – observed	Posterior – observed
ALF	3.0	1.3	1.2	0.7
SAN	2.3	1.3	1.3	0.6
RBA	4.1	1.3	1.5	0.7
TAB_TEF	3.5	1.4	1.4	0.7
	CARDAMOM as land–biosphere prior flux			
Site	Mean below 1.5 km altitude		Mean above 3.5 km altitude	
	Prior – observed	Posterior – observed	Prior – observed	Posterior – observed
ALF	−3.3	0.1	−2.1	−0.2
SAN	−2.9	0.0	−0.8	0.3
RBA	−5.9	−0.3	−2.5	0.1
TAB_TEF	−6.1	0.0	−1.5	0.3

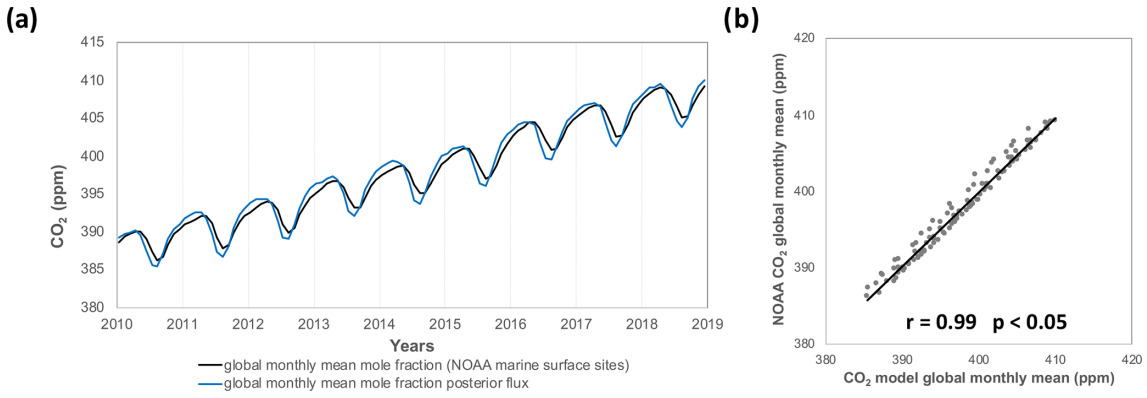

Figure A1. **(a)** Time series of the global monthly mean CO_2 mole fraction from our posteriori fluxes and from the NOAA marine surface sites (Lan et al., 2023). **(b)** Linear correlation between global monthly mean CO_2 mole fraction from our posteriori fluxes and from the NOAA marine surface sites.

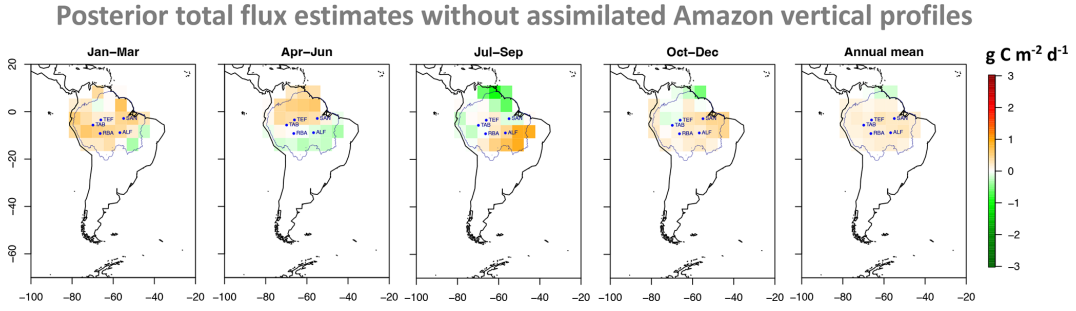

Figure A2. Quarterly and annual mean posterior total carbon fluxes without assimilated Amazon vertical profile data for the Amazon region between 2010 and 2018. The blue contour represents the Amazon area, based on Eva and Huber (2005).

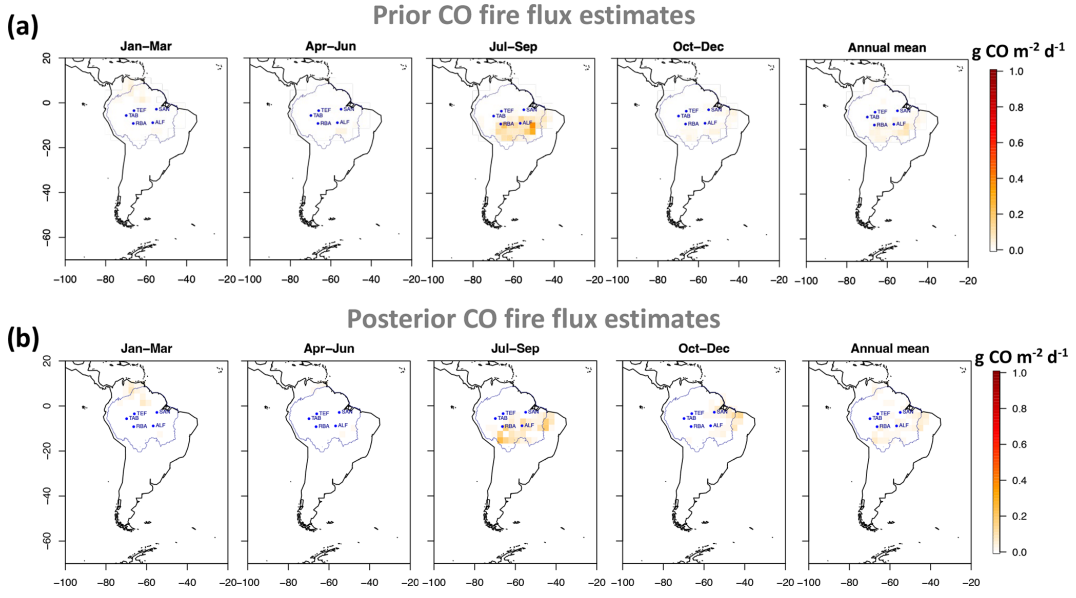

Figure A3. Quarterly and annual mean prior **(a)** and posterior **(b)** fire carbon monoxide (CO) fluxes with MOPITT data assimilated for the Amazon region between 2010 and 2018. The blue contour represents the Amazon area, based on Eva and Huber (2005).

Table A3. Annual mean fluxes (between April and December over the 9-year period, 2010 to 2018) using different CO estimates to estimate CO_2 fire and NBE fluxes.

Carbon fluxes (Pg C yr^{-1})		
Flux	NBE	Fire
CO_TOMCAT	0.02	0.24
CO_GFAS (Naus et al., 2022)	0.12	0.14
CO_opt (Naus et al., 2022)	0.04	0.22

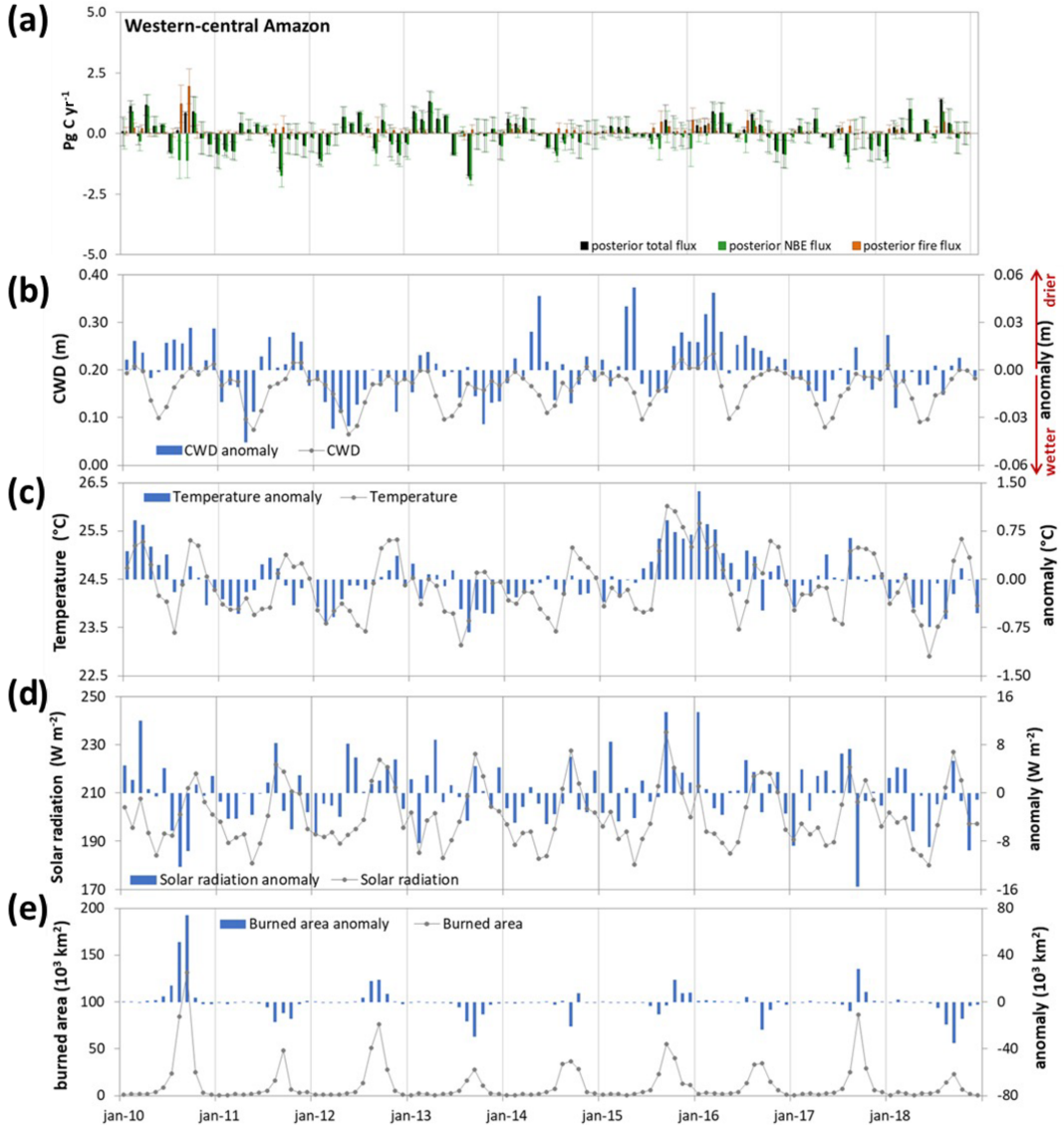

Figure A4. **(a)** Monthly mean carbon fluxes for the western-central Amazon area: posterior total flux with the Amazon vertical profile observations in the inversion (black bars), posterior fire fluxes using MOPITT carbon monoxide observations in the inversion (orange bars) and posterior NBE fluxes which are the result of the subtraction of the posterior fire fluxes from the posterior total fluxes with the Amazon vertical profile observations in the inversion (green bars), representing the net biome exchange. Monthly mean and anomalies of **(b)** cumulative water deficit (CWD), **(c)** temperature, **(d)** shortwave solar radiation downward flux (all sky) and **(e)** burned area for the western-central Amazon area.

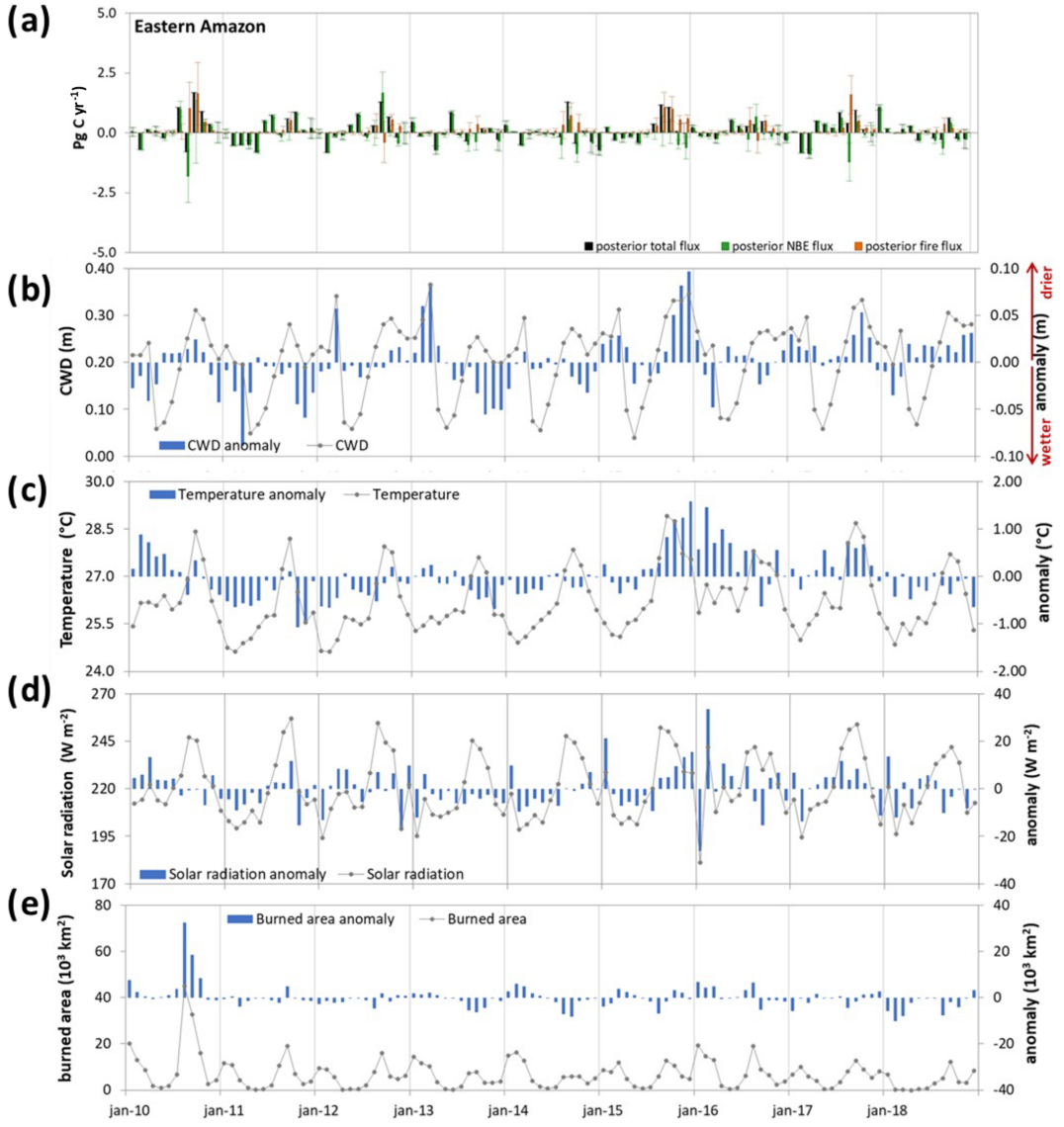

Figure A5. **(a)** Monthly mean carbon fluxes for the eastern Amazon area: posterior total flux with the Amazon vertical profile observations in the inversion (black bars), posterior fire fluxes using MOPITT carbon monoxide observations in the inversion (orange bars) and posterior NBE fluxes which are the result of the subtraction of the posterior fire fluxes from the posterior total fluxes with the Amazon vertical profile observations in the inversion (green bars), representing the net biome exchange. Monthly mean and anomalies of **(b)** cumulative water deficit (CWD), **(c)** temperature, **(d)** shortwave solar radiation downward flux (all sky) and **(e)** burned area for the eastern Amazon area.

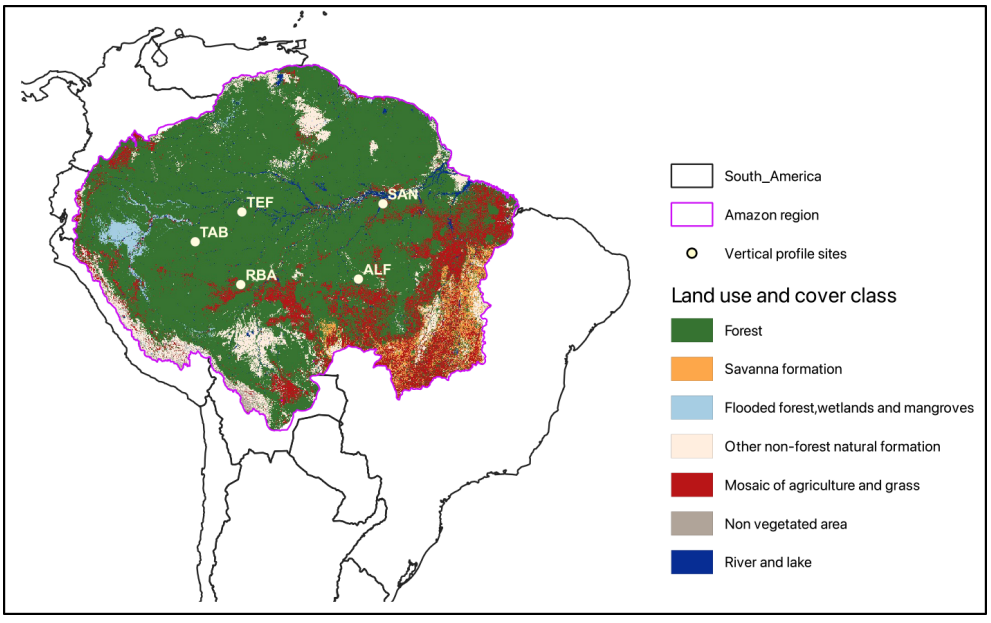

Figure A6. Map of land use and cover data from MapBiomas (2022) for Pan-Amazonia up to 2018. The purple line represents the Amazon region boundaries (based on Eva and Huber, 2005) and the grey line the South American boundaries.

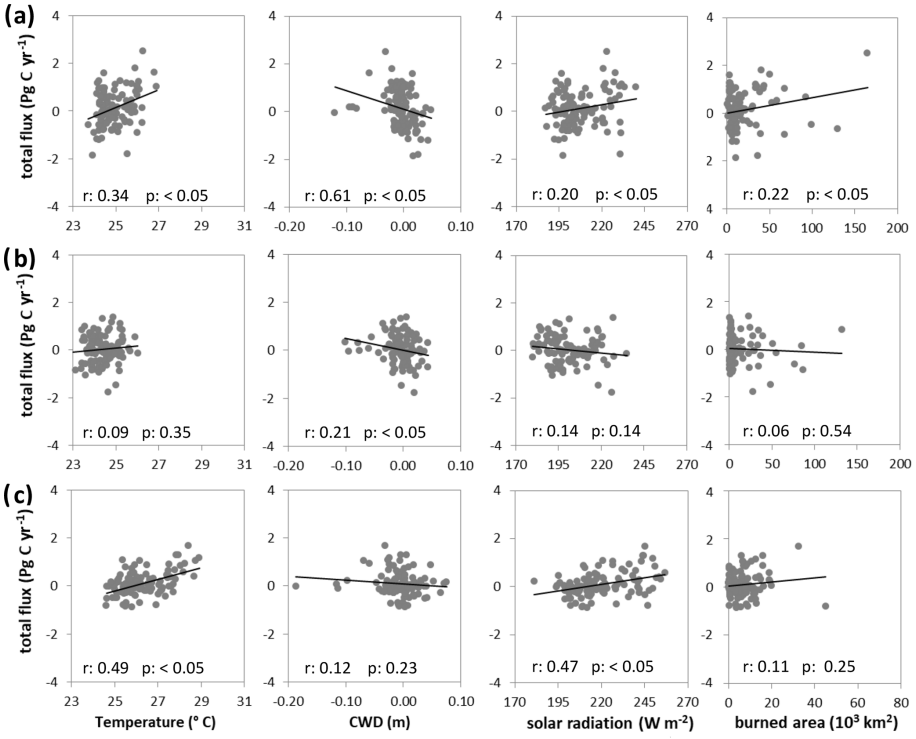

Figure A7. **(a)** Linear regressions between monthly mean carbon posterior total flux and temperature, cumulative water deficit (CWD), solar radiation and burned area for the **(a)** whole, **(b)** western-central and **(c)** eastern Amazon regions.

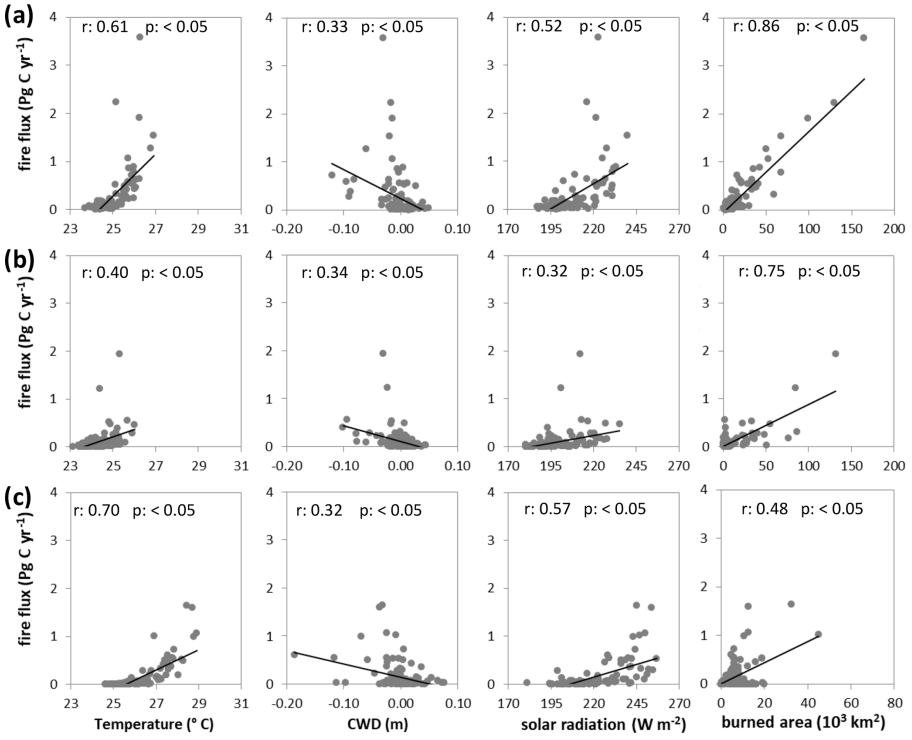

Figure A8. **(a)** Linear regressions between monthly mean carbon posterior fire flux and temperature, cumulative water deficit (CWD), solar radiation and burned area for the **(a)** whole, **(b)** western-central and **(c)** eastern Amazon regions.

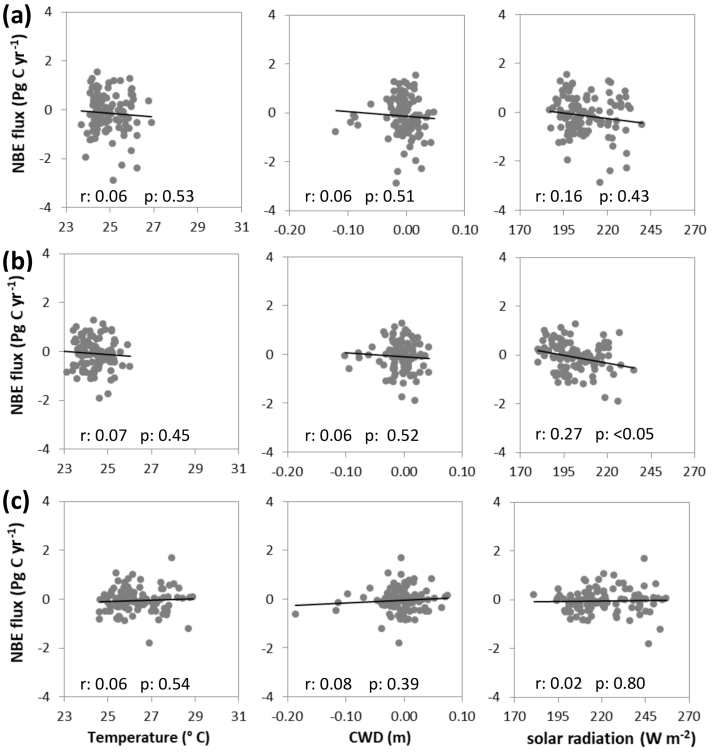

Figure A9. **(a)** Linear regressions between monthly mean carbon posterior NBE flux (posterior total flux less posterior fire flux) and temperature, cumulative water deficit (CWD) and solar radiation for the **(a)** whole, **(b)** western-central and **(c)** eastern Amazon regions.

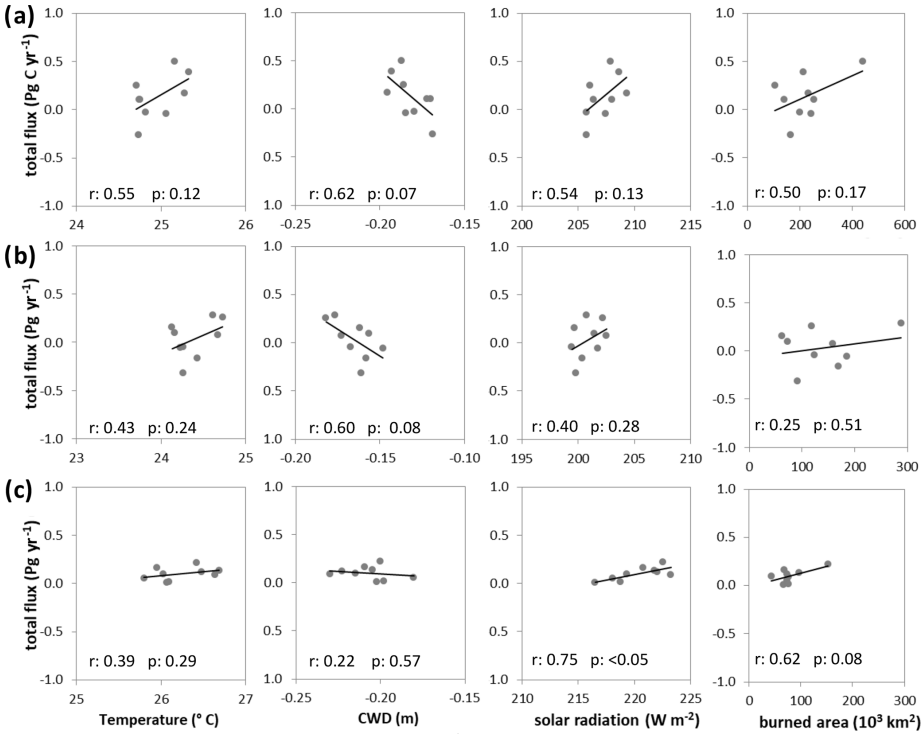

Figure A10. **(a)** Linear regressions between annual mean carbon posterior total flux (posterior total flux less posterior fire flux) and temperature, cumulative water deficit (CWD), solar radiation and burned area for the **(a)** whole, **(b)** western-central and **(c)** eastern Amazon regions.

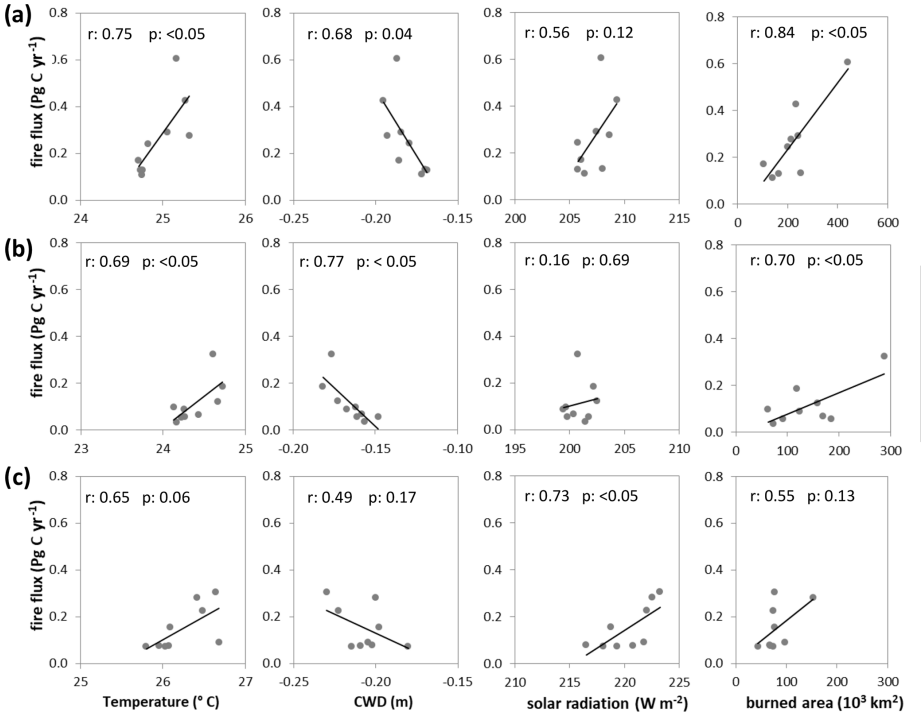

Figure A11. **(a)** Linear regressions between annual mean carbon posterior fire flux (posterior total flux less posterior fire flux) and temperature, cumulative water deficit (CWD), solar radiation and burned area for the **(a)** whole, **(b)** western-central and **(c)** eastern Amazon regions.

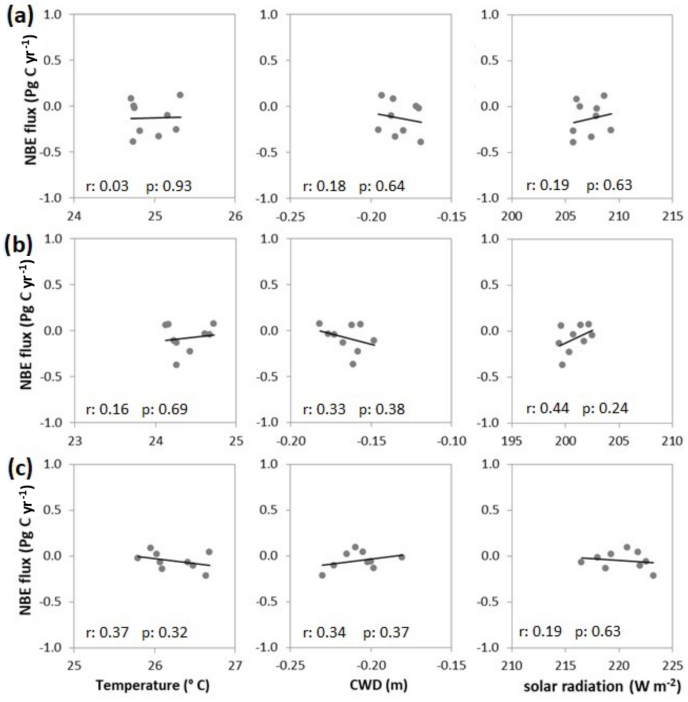

Figure A12. **(a)** Linear regressions between annual mean carbon posterior NBE flux (posterior total flux less posterior fire flux) and temperature, cumulative water deficit (CWD) and solar radiation for the **(a)** whole, **(b)** western-central and **(c)** eastern Amazon regions.

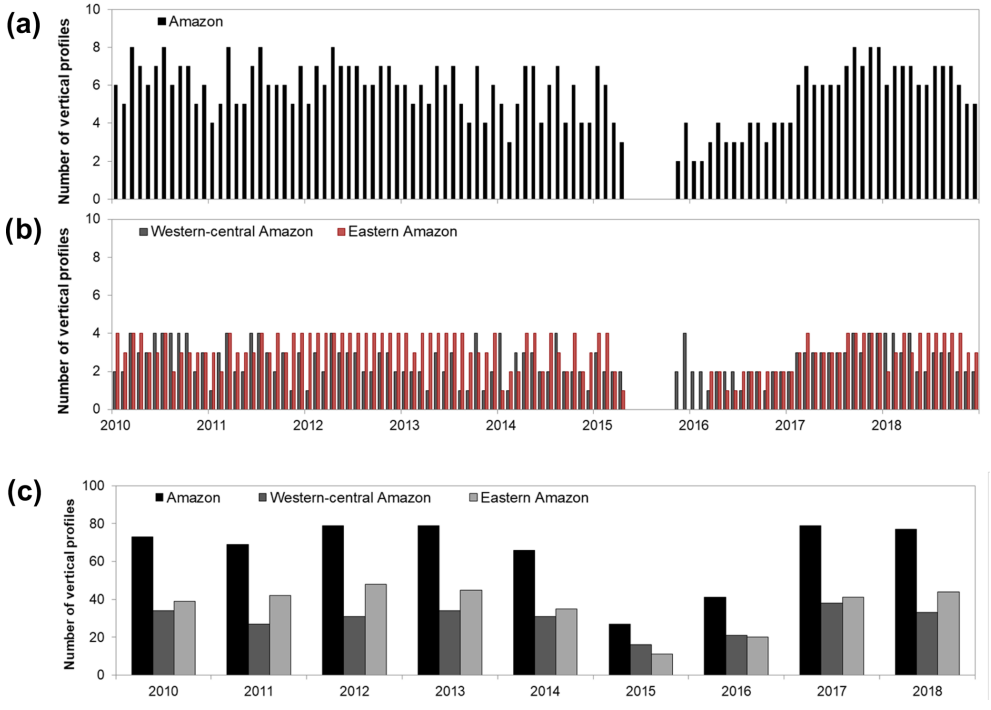

Figure A13. Total number of vertical profiles by month used in the inversions for the **(a)** whole Amazon area, **(b)** divided into the western-central (dark grey bars) and eastern Amazon regions (red bars). **(c)** Total number of vertical profiles for the whole (black bars), western-central (dark grey bars) and eastern Amazon regions (light grey bars). All the vertical profile data used were from Gatti et al. (2021a).

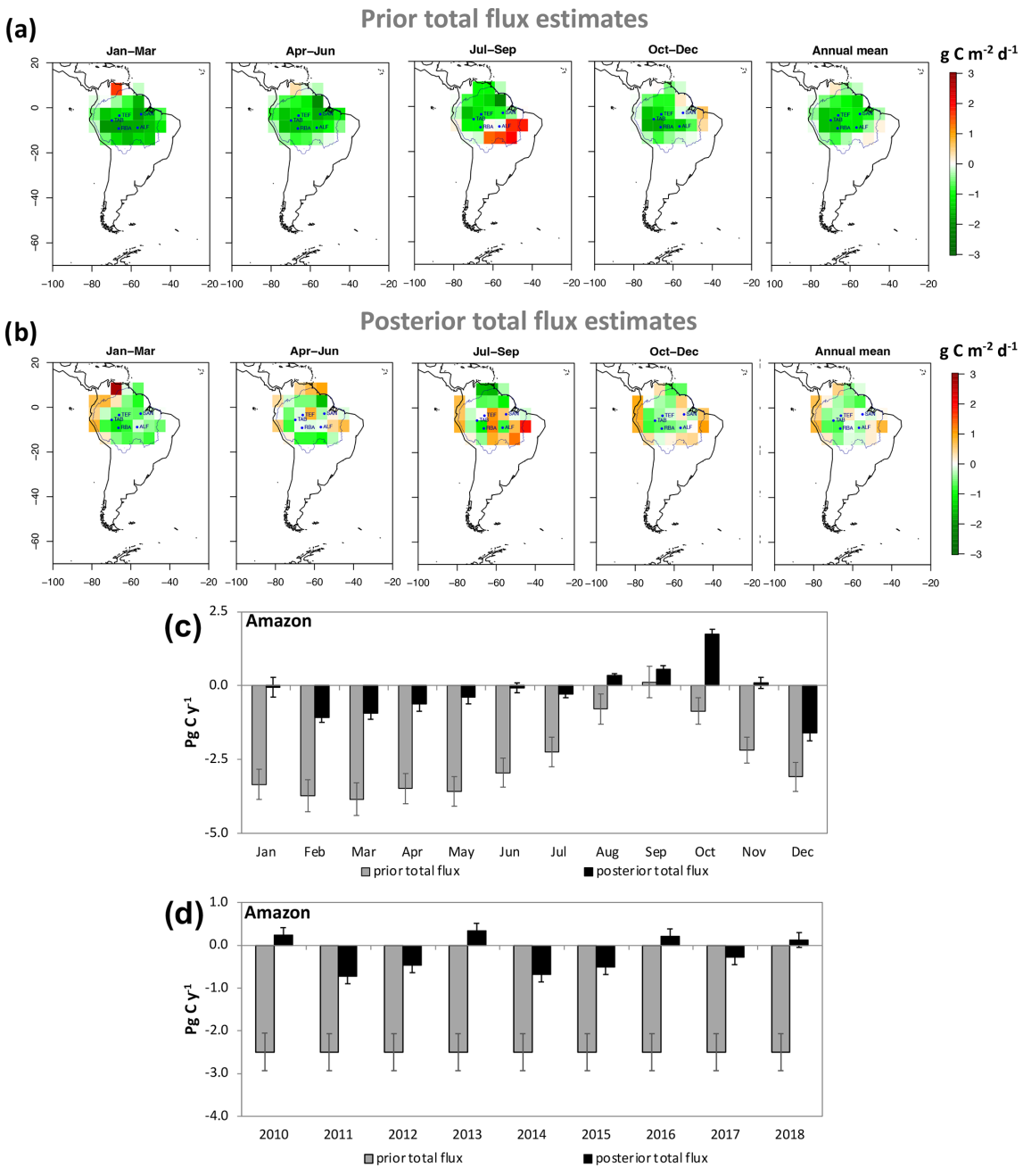

Figure A14. Quarterly and annual mean **(a)** prior total (with CARDAMOM as land–biosphere prior flux) and **(b)** posterior total (with CARDAMOM as land–biosphere prior flux) carbon fluxes, where a positive value indicates a net emission of C, while a negative value indicates a net uptake; **(c)** 9-year monthly mean and **(d)** annual mean carbon fluxes for the Amazon using CARDAMOM estimated as land–biosphere prior fluxes between 2010 and 2018. The blue contour represents the Amazon area, based on Eva and Huber (2005).

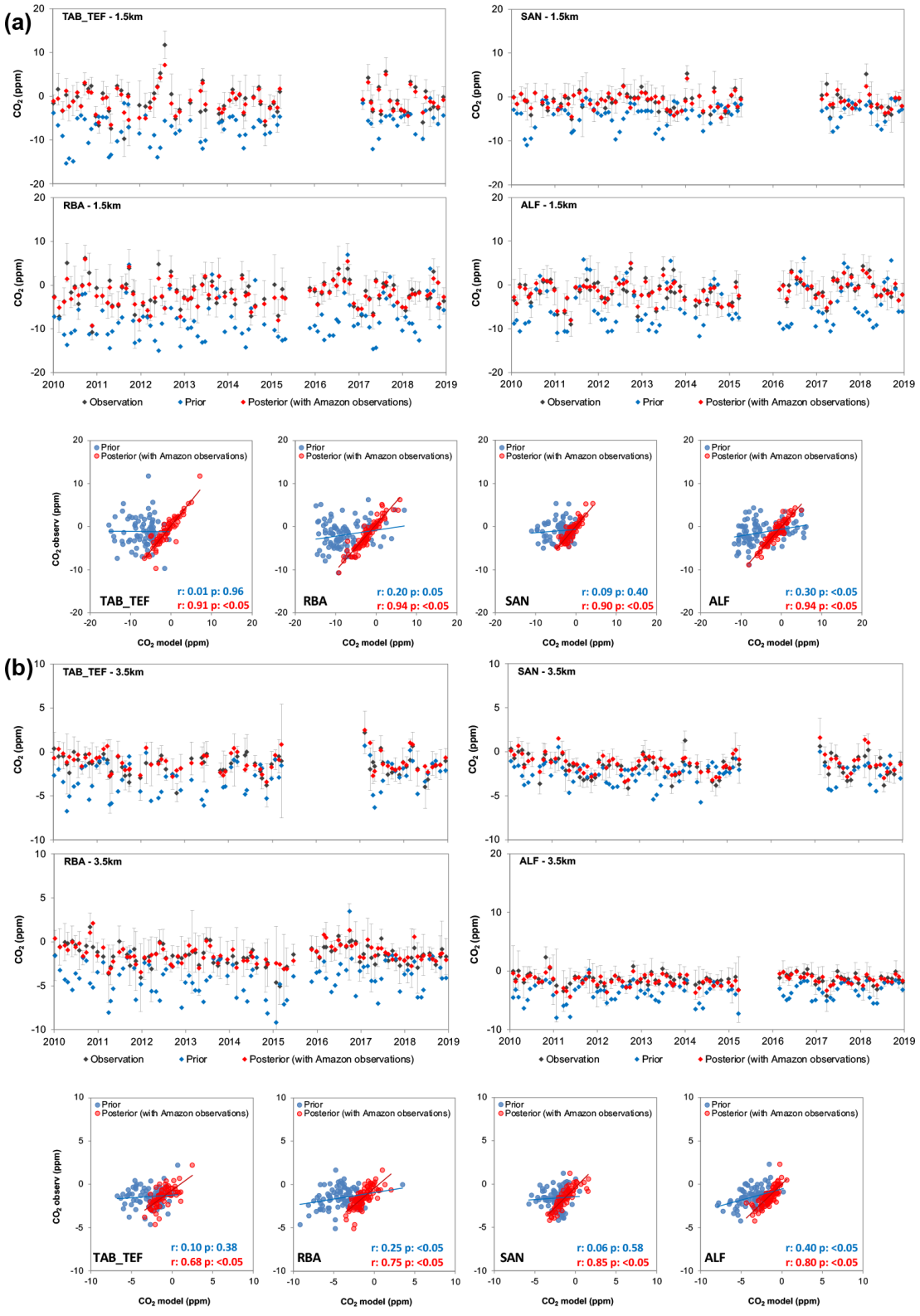

Figure A15. Detrended monthly mean CO_2 mole fractions (ppm) for prior (with CARDAMOM as land–biosphere prior flux), posterior and Amazon vertical profiles and its linear regressions, where panel **(a)** is the mean below 1.5 km altitude (planetary boundary layer levels) and **(b)** the mean above 3.5 km altitude (vertical profile free troposphere) for each of the vertical profile sites. The model results were extracted for the grid cell where each site is located. After detrending, we subtracted the global mean mole fraction from the observation and model mole fractions. Error bars represent the observation uncertainties.

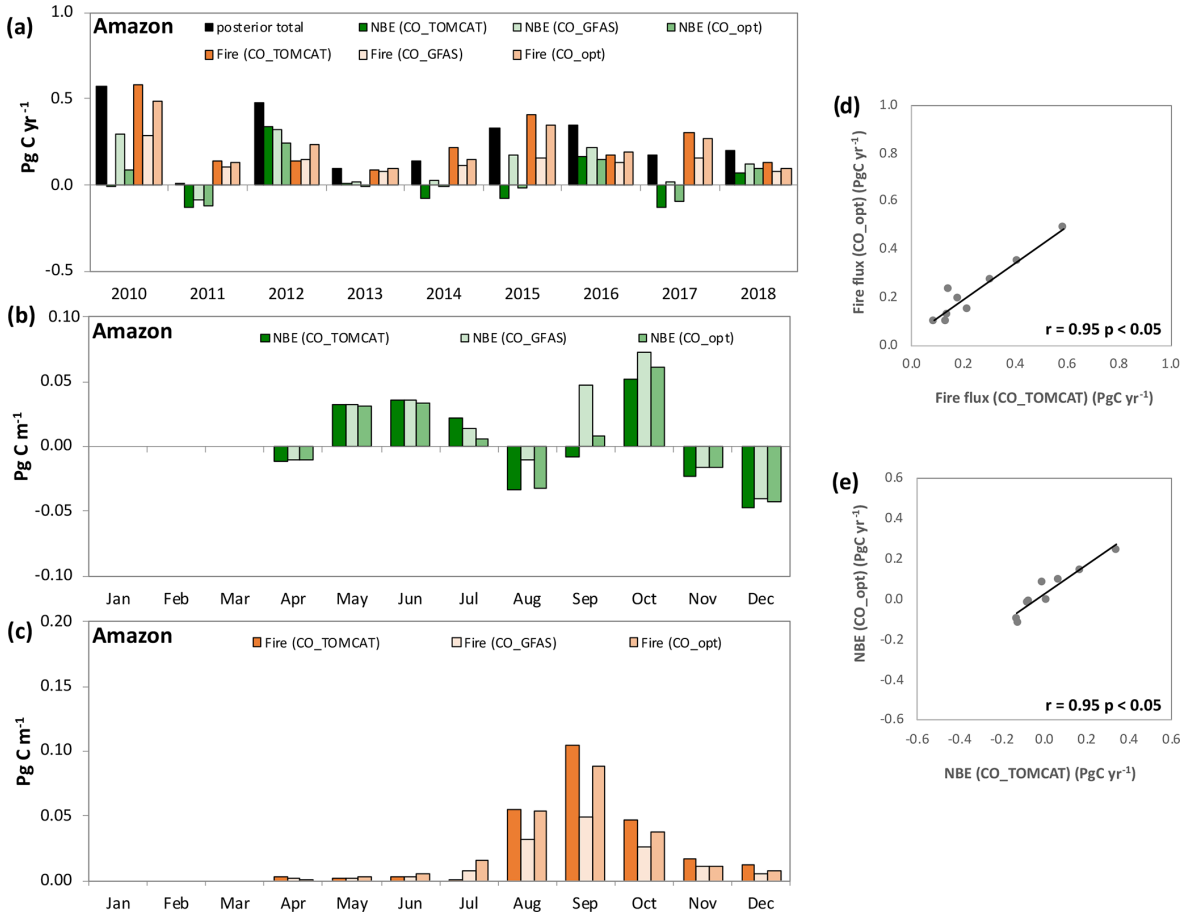

Figure A16. **(a)** Annual mean fluxes for the Amazon region total, fire and NBE estimates. Fire and NBE emissions based on TOMCAT CO inversions (CO_TOMCAT), Naus et al. (2022) emissions using GFAS as a prior (CO_GFAS) and emissions with their CO optimized inversions (CO_opt). The 9-year monthly mean NBE **(b)** and fire **(c)** carbon fluxes for the Amazon, fire and NBE based on TOMCAT CO inversions (CO_TOMCAT), Naus et al. (2022) emissions using GFAS as prior (CO_GFAS), and emissions with their CO optimized inversions (CO_opt). Linear regressions between annual mean carbon fire flux **(d)** and posterior NBE **(e)** based on TOMCAT CO inversions (CO_TOMCAT) and Naus et al. (2022) CO optimized inversions (CO_opt).

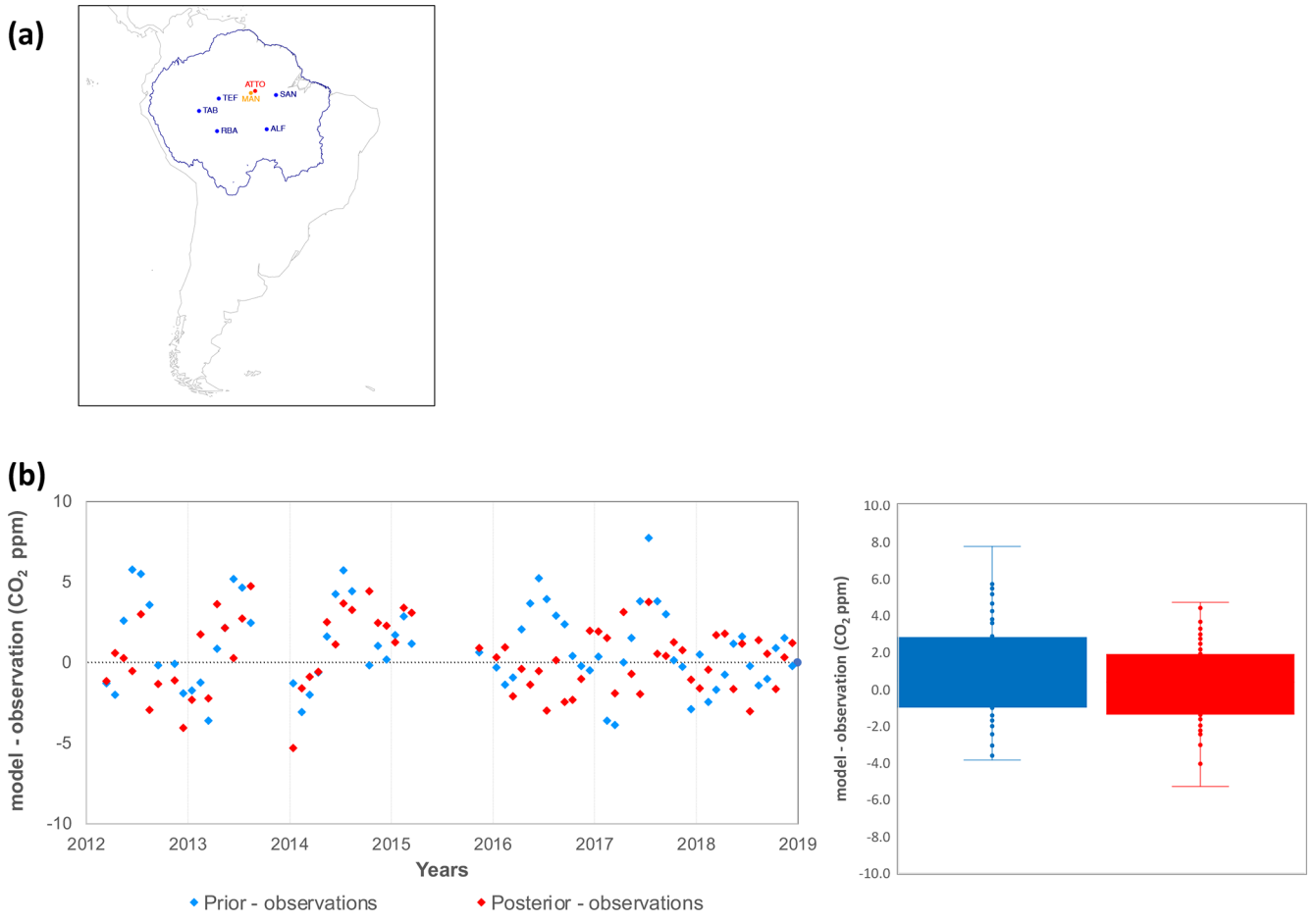

Figure A17. **(a)** Locations of LaGEE/INPE Amazon vertical profile sites assimilated in the inversions (blue circles) and the two sites (MAN and ATTO) with data used for cross-validation. The blue contour represents the Amazon area, based on Eva and Huber (2005). **(b)** Time series and box plot of the model bias (model – observations) of monthly mean CO_2 mole fractions (ppm) for the ATTO.

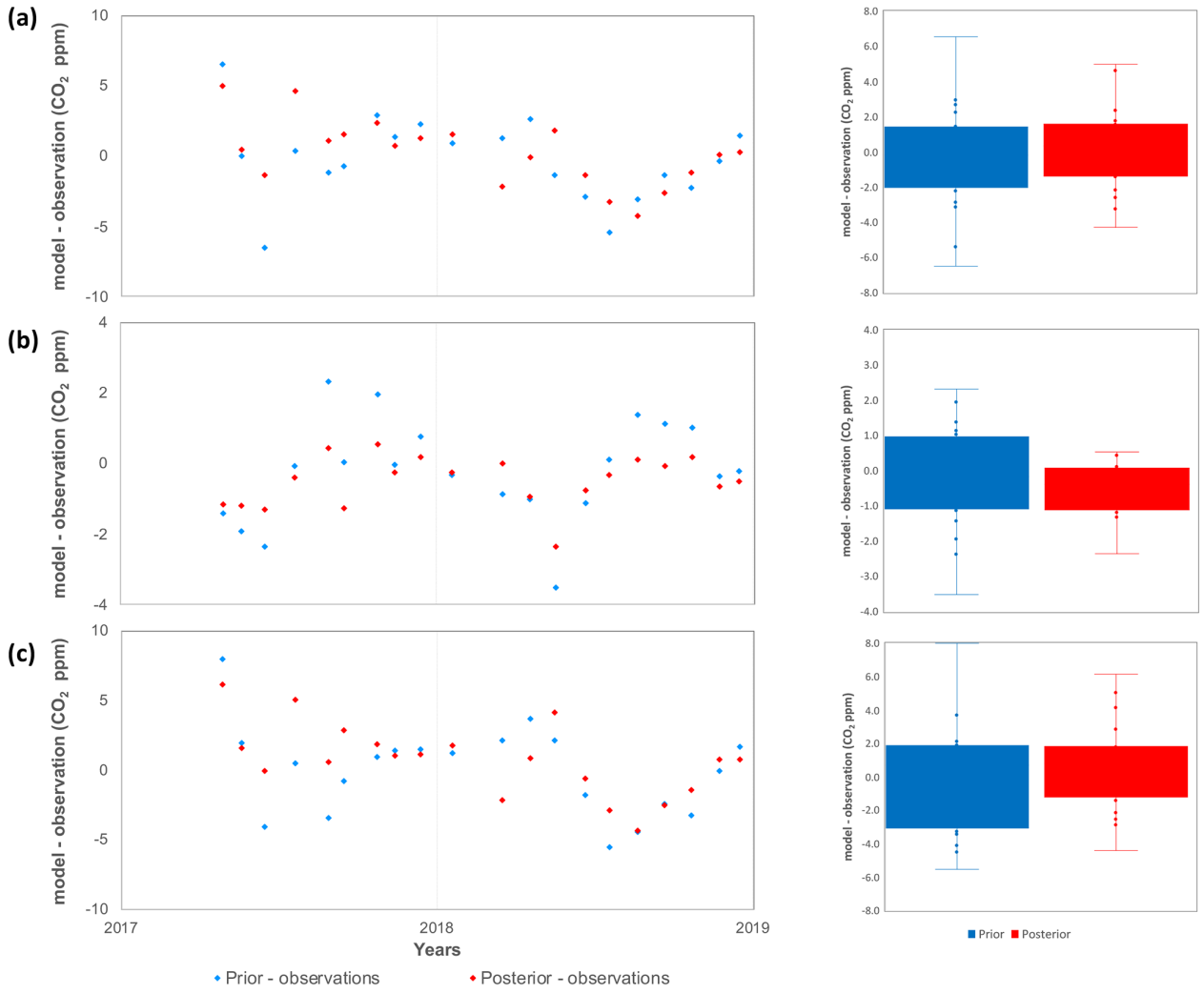

Figure A18. Time series and box plot of model bias (model – observations) of monthly mean CO_2 mole fractions (ppm) for the MAN vertical profiles **(a)** mean below 1.5 km, **(b)** mean above 3.5 km, and **(c)** difference between mean below 1.5 km and mean above 3.5 km.

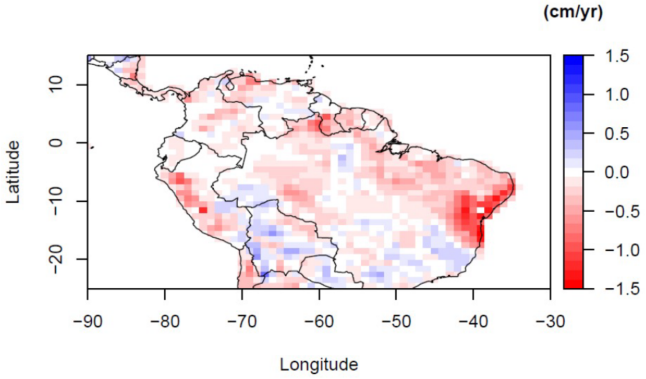

Figure A19. Time trend of maximum cumulative water deficit (CWD) between 1998 and 2019 based on TRMM v 7 precipitation estimates (Huffman et al., 2001).

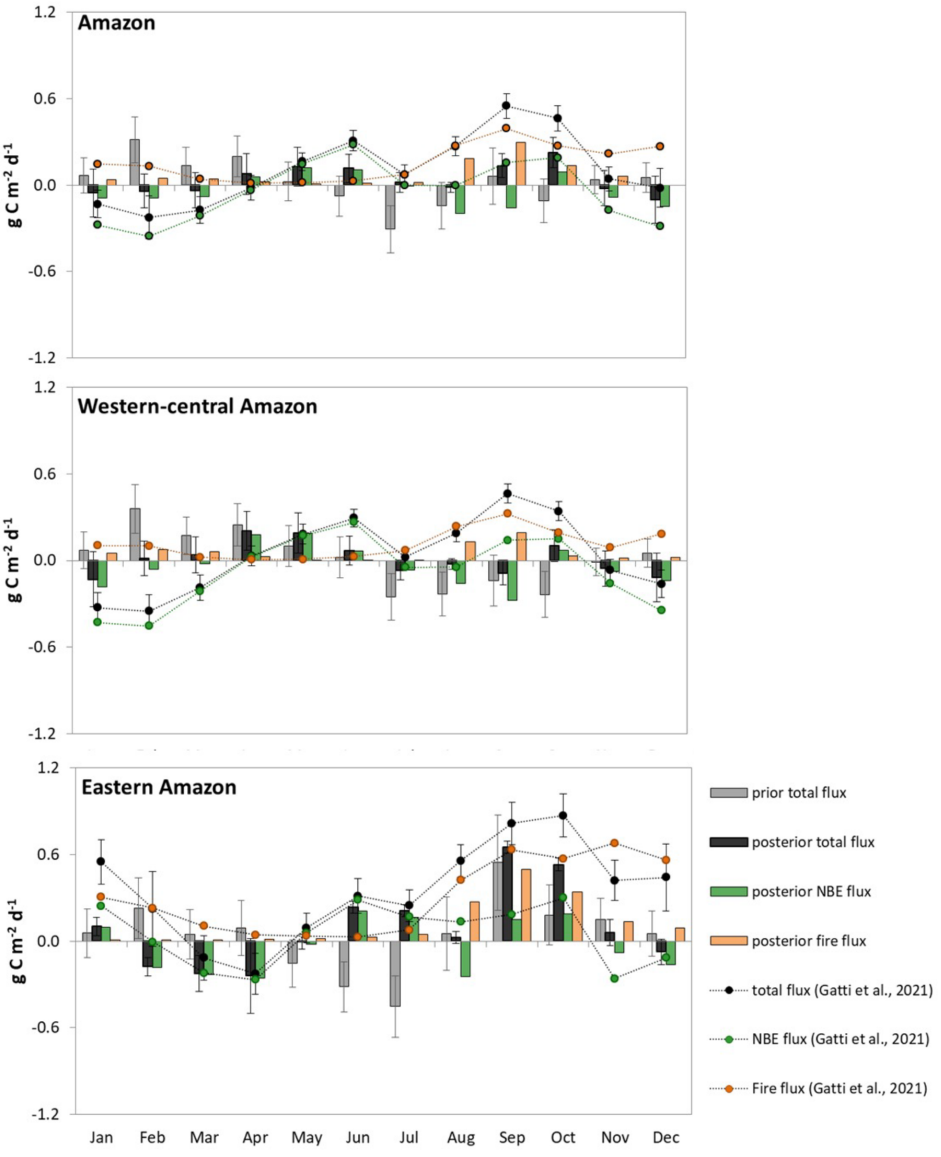

Figure A20. Comparison of monthly mean C fluxes from inverse modeling using Amazon vertical profile observations and C fluxes based the vertical profile observations calculated by mass balance technique from Gatti et al. (2021a), for the period between 2010 and 2018.

Code and data availability. The posterior CO fluxes from the atmospheric inversion can be made available upon request to Chris Wilson (c.wilson@leeds.ac.uk). Access to the CARDAMOM dataset can be granted upon request to T. Luke Smallman (t.l.smallman@ed.ac.uk). The prior and posterior mean South American CO_2 fluxes on the TOMCAT model grid are available from PANGAEA Data Archiving; the data DOI is https://doi.org/10.1594/PANGAEA.960593 (Basso et al., 2023). The vertical profile data used in this study are available at PANGAEA Data Archiving at https://doi.org/10.1594/PANGAEA.926834 (Gatti et al., 2021b). CO_2 global long-term surface data provided by the NOAA GML are available at https://doi.org/10.15138/wkgj-f215 (Lan et al., 2022). Fossil fuel emissions are from the Carbon Dioxide Information Analysis Center (CDIAC) (https://doi.org/10.3334/CDIAC/00001_V2017, Boden et al., 1999). CO_2 mole fractions from MAN aircraft vertical profiles are available at https://doi.org/10.25925/20210519 (Miller et al., 2021). Global Fire Emissions Database, Version 4 (GFEDv4), is available at https://doi.org/10.3334/ORNLDAAC/1293 (Randerson et al., 2017). Temperature data are from ERA-5 from the ECMWF (https://doi.org/10.24381/cds.f17050d7; Hersbach et al., 2023). Solar radiation data are from the Clouds and the Earth's Radiant Energy System (CERES-EBAF Ed4.1; https://ceres-tool.larc.nasa.gov/ord-tool/jsp/EBAF42Selection.jsp, CERES, 2022; Loeb et al., 2018; Kato et al., 2018). CO_2 mole fractions in the Amazon region made at the ATTO site are available upon request at https://www.attodata.org/ddm/data/Showdata/39 (Lavric and Walter, 2022a), https://www.attodata.org/ddm/data/Showdata/64 (Lavric and Walter, 2022b), https://www.attodata.org/ddm/data/Showdata/65 (Lavric and Walter, 2022c), https://www.attodata.org/ddm/data/Showdata/66 (Lavric and Walter, 2022d), https://www.attodata.org/ddm/data/Showdata/67 (Lavric and Walter, 2022e), https://www.attodata.org/ddm/data/Showdata/68 (Lavric and Walter, 2022f) and https://www.attodata.org/ddm/data/Showdata/69 (Lavric and Walter, 2022g).

Author contributions. LSB, CW, MG and MPC designed the methodology. LSB wrote the first version of the paper and performed the analysis and CO_2 inversions. CW performed the TOMCAT CO inversions using MOPITT data. GT provided the land use change data. HLGC and EA provided the burned area data. MW and TLS provided the CARDAMOM flux estimates. WP and SN provided the CO estimates for the sensitivity test. All authors contributed to the analysis and text.

Competing interests. The contact author has declared that none of the authors has any competing interests.

Disclaimer. Publisher's note: Copernicus Publications remains neutral with regard to jurisdictional claims in published maps and institutional affiliations.

Acknowledgements. Luana S. Basso, Henrique L. G. Cassol and Graciela Tejada acknowledge the financial support from São Paulo Research Foundation – FAPESP (2011/17914-0, 2018/14006-4, 2019/23654-2, 2018/14423-4, 2020/02656-4, 2018/18493-7). We acknowledge the support for this work from NERC grants AMAZONICA NE/F005806/1, BIO-RED NE/N012542/1 and ECOFOR NE/K01644X/1. Chris Wilson and Martyn P. Chipperfield acknowledge the contributions from the NERC National Centre for Earth Observation (NCEO). T. Luke Smallman and Mathew Williams were funded by the UK's National Centre for Earth Observation. The CARDAMOM analyses made use of the resources provided by the Edinburgh Compute and Data Facility (EDCF, http://www.ecdf.ed.ac.uk/, last access: 22 August 2023). The Amazon vertical profile database was funded by the São Paulo Research Foundation – FAPESP (2016/02018-2, 2011/51841-0, 2008/58120-3); the UK Natural Environmental Research Council (NERC) AMAZONICA project (NE/F005806/1); NASA grants (11-CMS11-0025, NRMJ1000-17-00431, NNX17AK49G); and the European Research Council (ERC) under Horizon 2020 (649087), 7FP EU (283080), MCTI/CNPq (2013) and CNPq (134878/2009-4). We thank the LaGEE/INPE team (the PI Luciana Gatti and the colleagues Luciano Marani, Caio C. S. C. Correia, Lucas G. Domingues, Raiane Neves and Stéphane Crispim) who provided the CO_2 data from the vertical profiles. In addition, we thank the pilots and technical team at the aircraft sites who collected the air samples. We thank numerous people at NOAA GML who provided the global station network CO_2 data, the ATTO research team who provided the CO_2 mole fraction data, and the MOPITT team who provided the CO total column data.

Financial support. This research has been supported by the State of Sao Paulo Science Foundation (grant nos. 2016/02018-2, 2018/14006-4, 2018/14423-4, 2018/18493-7, 2019/23654-2 and 2020/02656-4), the Natural Environment Research Council (grant nos. AMAZONICA NE/F005806/1, BIO-RED NE/N012542/1, and ECOFOR NE/K01644X/1), the NERC National Centre for Earth Observation (NCEO), the UK's National Centre for Earth Observation, the State of Sao Paulo Science Foundation – FAPESP (2016/02018-2, 2011/51841-0, 2008/58120-3, 2018/14423-4, 2018/18493-7, 2019/21789-8, 2019/23654-2), the UK Natural Environmental Research Council (NERC) AMAZONICA project (grant no. NE/F005806/1), NASA grants (grant nos. 11-CMS11-0025, NRMJ1000-17-00431, NNX17AK49G), and the European Research Council (ERC) under Horizon 2020 (grant no. 649087), 7FP EU(grant no. 283080), MCTI/CNPq (grant no. 2013) and CNPq (grant no. 134878/2009-4).

Review statement. This paper was edited by Abhishek Chatterjee and reviewed by two anonymous referees.

References

Alden, C. B., Miller, J. B., Gatti, L. V., Gloor, M. M., Guan, K., Michalak, A. M., van der Laan-Luijkx, I. T., Touma, D., Andrews, A., Basso, L. S., Correia, C. S. C., Domingues, L. G., Joiner, J., Krol, M. C., Lyapustin, A. I., Peters, W., Shiga, Y. P., Thoning, K., van der Velde, I. R., van Leeuwen, T. T., Yadav, V., and Diffenbaugh, N. S.: Regional atmospheric CO_2 inversion reveals seasonal and geographic differences in Amazon net biome exchange, Glob. Chang. Biol., 22, 3427–3443, https://doi.org/10.1111/gcb.13305, 2016.

Anderson, L. O., Aragão, L. E. O. C., Gloor, M., Arai, E., Adami, M., Saatchi, S. S., Malhi, Y., Shimabukuro, Y. E., Barlow, J., Berenguer, E., and Duarte, V.: Disentangling the contribution of multiple land covers to fire-mediated carbon emissions in Amazonia during the 2010 drought, Global Biogeochem. Cy., 29, 1739–1753, https://doi.org/10.1002/2014GB005008, 2015.

Anderson, L. O., Neto, G. R., Cunha, A. P., Fonseca, M. G., De Moura, Y. M., Dalagnol, R., Wagner, F. H., and De Aragão, L. E. O. E. C.: Vulnerability of Amazonian forests to repeated droughts, Philos. T. Roy. Soc. B, 373, 20170411, https://doi.org/10.1098/rstb.2017.0411, 2018.

Aragão, L. E. O. C., Anderson, L. O., Fonseca, M. G., Rosan, T. M., Vedovato, L. B., Wagner, F. H., Silva, C. V. J., Silva Junior, C. H. L., Arai, E., Aguiar, A. P., Barlow, J., Berenguer, E., Deeter, M. N., Domingues, L. G., Gatti, L., Gloor, M., Malhi, Y., Marengo, J. A., Miller, J. B., Phillips, O. L., and Saatchi, S.: 21st Century drought-related fires counteract the decline of Amazon deforestation carbon emissions, Nat. Commun., 9, 536, https://doi.org/10.1038/s41467-017-02771-y, 2018.

Baier, B. C., Sweeney, C., Choi, Y., Davis, K. J., DiGangi, J. P., Feng, S., Fried, A., Halliday, H., Higgs, J., Lauvaux, T., Miller, B. R., Montzka, S. A., Newberger, T., Nowak, J. B., Patra, P., Richter, D., Walega, J., and Weibring, P.: Multispecies Assessment of Factors Influencing Regional CO_2 and CH_4 Enhancements During the Winter 2017 ACT-America Campaign, J. Geophys. Res.-Atmos., 125, e2019JD031339, https://doi.org/10.1029/2019JD031339, 2020.

Baret, F., Weiss, M., Verger, A., and Smets, B.: Atbd for Lai, Fapar and Fcover From Proba-V Products at 300 m Resolution (Geov3), INRA, Paris, France, https://land.copernicus.eu/global/sites/cgls.vito.be/files/products/ImagineS_RP2.1_ATBD-FAPAR300m_I1.73.pdf (last access: 22 August 2023), 2016.

Basso, L. S., Wilson, C., Chipperfield, M. P., and Gloor, M.: Posterior Amazon monthly mean surface carbon flux between 2010 and 2018 estimated using the INVICAT 4D-Var inverse model, PANGAEA [data set], https://doi.org/10.1594/PANGAEA.960593, 2023.

Berenguer, E., Carvalho, N., Anderson, L. O., Aragão, L. E. O. C., França, F., and Barlow, J.: Improving the spatial-temporal analysis of Amazonian fires, Glob. Chang. Biol., 27, 469–471, https://doi.org/10.1111/gcb.15425, 2021.

Bloom, A. A., Exbrayat, J.-F., van der Velde, I. R., Feng, L., and Williams, M.: The decadal state of the terrestrial carbon cycle: Global retrievals of terrestrial carbon allocation, pools, and residence times, P. Natl. Acad. Sci. USA, 113, 1285–1290, https://doi.org/10.1073/pnas.1515160113, 2016.

Boden, T., Marland, G., and Andres, R. J.: Global, Regional, and National Fossil-Fuel CO_2 Emissions (1751–2014) (V. 2017), Carbon Dioxide Information Analysis Center (CDIAC), Oak Ridge National Laboratory (ORNL), Oak Ridge, TN (United States), ESS-DIVE repository [data set], https://doi.org/10.3334/CDIAC/00001_V2017, 1999.

Botía, S., Komiya, S., Marshall, J., Koch, T., Gałkowski, M., Lavric, J., Gomes-Alves, E., Walter, D., Fisch, G., Pinho, D. M., Nelson, B. W., Martins, G., Luijkx, I. T., Koren, G., Florentie, L., Carioca de Araújo, A., Sá, M., Andreae, M. O., Heimann, M., Peters, W., and Gerbig, C.: The CO_2 record at the Amazon Tall Tower Observatory: A new opportunity to study processes on seasonal and inter-annual scales, Glob. Chang. Biol., 28, 588–611, https://doi.org/10.1111/gcb.15905, 2022.

Botía Bocanegra, S.: Greenhouse gas exchange in the Amazon region: carbon dioxide and methane insights from the Amazon Tall Tower Observatory (ATTO), PhD thesis, Wageningen University, https://doi.org/10.18174/573967, 2022.

Bousserez, N., Henze, D. K., Perkins, A., Bowman, K. W., Lee, M., Liu, J., Deng, F., and Jones, D. B. A.: Improved analysis-error covariance matrix for high-dimensional variational inversions: application to source estimation using a 3D atmospheric transport model, Q. J. Roy. Meteor. Soc., 141, 1906–1921, https://doi.org/10.1002/qj.2495, 2015.

Brando, P., Macedo, M., Silvério, D., Rattis, L., Paolucci, L., Alencar, A., Coe, M., and Amorim, C.: Amazon wildfires: Scenes from a foreseeable disaster, Flora, 268, 151609, https://doi.org/10.1016/j.flora.2020.151609, 2020.

Brienen, R. J. W., Phillips, O. L., Feldpausch, T. R., Gloor, E., Baker, T. R., Lloyd, J., Lopez-Gonzalez, G., Monteagudo-Mendoza, A., Malhi, Y., Lewis, S. L., Vásquez Martinez, R., Alexiades, M., Álvarez Dávila, E., Alvarez-Loayza, P., Andrade, A., Aragaõ, L. E. O. C., Araujo-Murakami, A., Arets, E. J. M. M., Arroyo, L., Aymard C., G. A., Bánki, O. S., Baraloto, C., Barroso, J., Bonal, D., Boot, R. G. A., Camargo, J. L. C., Castilho, C. V., Chama, V., Chao, K. J., Chave, J., Comiskey, J. A., Cornejo Valverde, F., Da Costa, L., De Oliveira, E. A., Di Fiore, A., Erwin, T. L., Fauset, S., Forsthofer, M., Galbraith, D. R., Grahame, E. S., Groot, N., Hérault, B., Higuchi, N., Honorio Coronado, E. N., Keeling, H., Killeen, T. J., Laurance, W. F., Laurance, S., Licona, J., Magnussen, W. E., Marimon, B. S., Marimon-Junior, B. H., Mendoza, C., Neill, D. A., Nogueira, E. M., Núñez, P., Pallqui Camacho, N. C., Parada, A., Pardo-Molina, G., Peacock, J., Penã-Claros, M., Pickavance, G. C., Pitman, N. C. A., Poorter, L., Prieto, A., Quesada, C. A., Ramírez, F., Ramírez-Angulo, H., Restrepo, Z., Roopsind, A., Rudas, A., Salomaõ, R. P., Schwarz, M., Silva, N., Silva-Espejo, J. E., Silveira, M., Stropp, J., Talbot, J., Ter Steege, H., Teran-Aguilar, J., Terborgh, J., Thomas-Caesar, R., Toledo, M., Torello-Raventos, M., Umetsu, R. K., Van Der Heijden, G. M. F., Van Der Hout, P., Guimarães Vieira, I. C., Vieira, S. A., Vilanova, E., Vos, V. A., and Zagt, R. J.: Long-term decline of the Amazon carbon sink, Nature, 519, 344–348, https://doi.org/10.1038/nature14283, 2015.

Chipperfield, M. P.: New version of the TOMCAT/SLIMCAT off-line chemical transport model: Intercomparison of stratospheric tracer experiments, Q. J. Roy. Meteor. Soc., 132, 1179–1203, https://doi.org/10.1256/QJ.05.51, 2006.

Clouds and the Earth's Radiant Energy System (CERES): Energy Balanced and Filled (EBAF) data product, Edition 4.2,

CERES [data set], https://ceres-tool.larc.nasa.gov/ord-tool/jsp/EBAF42Selection.jsp, last access: 30 July 2022.

Dee, D. P., Uppala, S. M., Simmons, A. J., Berrisford, P., Poli, P., Kobayashi, S., Andrae, U., Balmaseda, M. A., Balsamo, G., Bauer, P., Bechtold, P., Beljaars, A. C. M., van de Berg, L., Bidlot, J., Bormann, N., Delsol, C., Dragani, R., Fuentes, M., Geer, A. J., Haimberger, L., Healy, S. B., Hersbach, H., Hólm, E. V., Isaksen, L., Kållberg, P., Köhler, M., Matricardi, M., Mcnally, A. P., Monge-Sanz, B. M., Morcrette, J. J., Park, B. K., Peubey, C., de Rosnay, P., Tavolato, C., Thépaut, J. N., and Vitart, F.: The ERA-Interim reanalysis: configuration and performance of the data assimilation system, Q. J. Roy. Meteor. Soc., 137, 553–597, https://doi.org/10.1002/QJ.828, 2011.

Deeter, M. N., Edwards, D. P., Francis, G. L., Gille, J. C., Mao, D., Martínez-Alonso, S., Worden, H. M., Ziskin, D., and Andreae, M. O.: Radiance-based retrieval bias mitigation for the MOPITT instrument: the version 8 product, Atmos. Meas. Tech., 12, 4561–4580, https://doi.org/10.5194/amt-12-4561-2019, 2019.

Domingues, L. G., Gatti, L. V., Aquino, A., Sánchez, A., Correia, C., Gloor, M., Peters, W., Miller, J., Turnbull, J., Santana, R., Marani, L., Câmara, G., Neves, R., and Crispim, S.: A new background method for greenhouse gases flux calculation based in back-trajectories over the Amazon, Atmosphere, 11, 734, https://doi.org/10.3390/atmos11070734, 2020.

Eva, H. D. and Huber, O.: A Proposal for Defining the Geographical Boundaries of Amazonia: Synthesis of the results from an Expert Consultation Workshop organized by the European Commission in collaboration with the Amazon Cooperation Treaty Organization – JRC, 7–8 June 2005, Ispra, Italy, European Comission – Joint Research Centre (JRC), ISBN 92-79-00012-8, 2005.

Exbrayat, J., Smallman, T. L., Bloom, A. A., Hutley, L. B., and Williams, M.: Inverse Determination of the Influence of Fire on Vegetation Carbon Turnover in the Pantropics, Global Biogeochem. Cy., 32, 1776–1789, https://doi.org/10.1029/2018GB005925, 2018.

Fancourt, M., Ziv, G., Boersma, K. F., Tavares, J., Wang, Y., and Galbraith, D.: Background climate conditions regulated the photosynthetic response of Amazon forests to the 2015/2016 El Nino-Southern Oscillation event, Commun. Earth Environ., 3, 1–9, https://doi.org/10.1038/s43247-022-00533-3, 2022.

Fawcett, D., Sitch, S., Ciais, P., Wigneron, J. P., Silva-Junior, C. H. L., Heinrich, V., Vancutsem, C., Achard, F., Bastos, A., Yang, H., Li, X., Albergel, C., Friedlingstein, P., and Aragão, L. E. O. C.: Declining Amazon biomass due to deforestation and subsequent degradation losses exceeding gains, Glob. Chang. Biol., 29, 1106–1118, https://doi.org/10.1111/gcb.16513, 2023.

Friedl, M. A., Sulla-Menashe, D., Tan, B., Schneider, A., Ramankutty, N., Sibley, A., and Huang, X.: MODIS Collection 5 global land cover: Algorithm refinements and characterization of new datasets, Remote Sens. Environ., 114, 168–182, https://doi.org/10.1016/j.rse.2009.08.016, 2010.

Friedlingstein, P., O'Sullivan, M., Jones, M. W., Andrew, R. M., Hauck, J., Olsen, A., Peters, G. P., Peters, W., Pongratz, J., Sitch, S., Le Quéré, C., Canadell, J. G., Ciais, P., Jackson, R. B., Alin, S., Aragão, L. E. O. C., Arneth, A., Arora, V., Bates, N. R., Becker, M., Benoit-Cattin, A., Bittig, H. C., Bopp, L., Bultan, S., Chandra, N., Chevallier, F., Chini, L. P., Evans, W., Florentie, L., Forster, P. M., Gasser, T., Gehlen, M., Gilfillan, D., Gkritzalis, T., Gregor, L., Gruber, N., Harris, I., Hartung, K., Haverd, V., Houghton, R. A., Ilyina, T., Jain, A. K., Joetzjer, E., Kadono, K., Kato, E., Kitidis, V., Korsbakken, J. I., Landschützer, P., Lefèvre, N., Lenton, A., Lienert, S., Liu, Z., Lombardozzi, D., Marland, G., Metzl, N., Munro, D. R., Nabel, J. E. M. S., Nakaoka, S.-I., Niwa, Y., O'Brien, K., Ono, T., Palmer, P. I., Pierrot, D., Poulter, B., Resplandy, L., Robertson, E., Rödenbeck, C., Schwinger, J., Séférian, R., Skjelvan, I., Smith, A. J. P., Sutton, A. J., Tanhua, T., Tans, P. P., Tian, H., Tilbrook, B., van der Werf, G., Vuichard, N., Walker, A. P., Wanninkhof, R., Watson, A. J., Willis, D., Wiltshire, A. J., Yuan, W., Yue, X., and Zaehle, S.: Global Carbon Budget 2020, Earth Syst. Sci. Data, 12, 3269–3340, https://doi.org/10.5194/essd-12-3269-2020, 2020.

Friedlingstein, P., Jones, M. W., O'Sullivan, M., Andrew, R. M., Bakker, D. C. E., Hauck, J., Le Quéré, C., Peters, G. P., Peters, W., Pongratz, J., Sitch, S., Canadell, J. G., Ciais, P., Jackson, R. B., Alin, S. R., Anthoni, P., Bates, N. R., Becker, M., Bellouin, N., Bopp, L., Chau, T. T. T., Chevallier, F., Chini, L. P., Cronin, M., Currie, K. I., Decharme, B., Djeutchouang, L. M., Dou, X., Evans, W., Feely, R. A., Feng, L., Gasser, T., Gilfillan, D., Gkritzalis, T., Grassi, G., Gregor, L., Gruber, N., Gürses, Ö., Harris, I., Houghton, R. A., Hurtt, G. C., Iida, Y., Ilyina, T., Luijkx, I. T., Jain, A., Jones, S. D., Kato, E., Kennedy, D., Klein Goldewijk, K., Knauer, J., Korsbakken, J. I., Körtzinger, A., Landschützer, P., Lauvset, S. K., Lefèvre, N., Lienert, S., Liu, J., Marland, G., McGuire, P. C., Melton, J. R., Munro, D. R., Nabel, J. E. M. S., Nakaoka, S.-I., Niwa, Y., Ono, T., Pierrot, D., Poulter, B., Rehder, G., Resplandy, L., Robertson, E., Rödenbeck, C., Rosan, T. M., Schwinger, J., Schwingshackl, C., Séférian, R., Sutton, A. J., Sweeney, C., Tanhua, T., Tans, P. P., Tian, H., Tilbrook, B., Tubiello, F., van der Werf, G. R., Vuichard, N., Wada, C., Wanninkhof, R., Watson, A. J., Willis, D., Wiltshire, A. J., Yuan, W., Yue, C., Yue, X., Zaehle, S., and Zeng, J.: Global Carbon Budget 2021, Earth Syst. Sci. Data, 14, 1917–2005, https://doi.org/10.5194/essd-14-1917-2022, 2022.

Gatti, L. V., Gloor, M., Miller, J. B., Doughty, C. E., Malhi, Y., Domingues, L. G., Basso, L. S., Martinewski, A., Correia, C. S. C., Borges, V. F., Freitas, S., Braz, R., Anderson, L. O., Rocha, H., Grace, J., Phillips, O. L., and Lloyd, J.: Drought sensitivity of Amazonian carbon balance revealed by atmospheric measurements, Nature, 506, 76–80, https://doi.org/10.1038/nature12957, 2014.

Gatti, L. V., Basso, L. S., Miller, J. B., Gloor, M., Domingues, L. G., Cassol, H. L. G., Tejada, G., Aragão, L. E. O. C., Nobre, C., Peters, W., Marani, L., Arai, E., Sanches, A. H., Correa, S. M., Anderson, L., Von Randon, C., Correia, C. S. C., Crispim, S. P., and Neves, R. A. L.: Amazonia as a carbon source linked to deforestation and climate change, Nature, 595, 388–393, https://doi.org/10.1038/s41586-021-03629-6, 2021a.

Gatti, L. V., Correa, C. C. S., Domingues, L. G., Miller, J. B., Gloor, M., Martinewski, A., Basso, L. S., Santana, R., Crispim, S. P., Marani, L., and Neves, R. L.: CO_2 Vertical Profiles on Four Sites over Amazon from 2010 to 2018, PANGAEA [data set], https://doi.org/10.1594/PANGAEA.926834, 2021b.

Gatti, L. V., Melack, J., Basso, L. S., Restrepo-Coupe, N., Aguiar, A. P., Pangala, S., Saleska, S. R., Aragão, L., Phillips, O. L., and Armenteras, D: Cross-Chapter 1: The Amazon Carbon Budget, in: Amazon Assessment Report 2021, edited by: Nobre, C., Encalada, A., Anderson, E., Roca Alcazar, F. H., Bustamante, M., Mena, C., Peña-Claros, M., Poveda, G., Rodriguez, J. P., Saleska,

S., Trumbore, S., Val, A. L., Villa Nova, L., Abramovay, R., Alencar, A., Rodríguez Alzza, C., Armenteras, D., Artaxo, P., Athayde, S., Barretto Filho, H. T., Barlow, J., Berenguer, E., Bortolotto, F., Costa, F. A., Costa, M. H., Cuvi, N., Fearnside, P. M., Ferreira, J., Flores, B. M., Frieri, S., Gatti, L. V., Guayasamin, J. M., Hecht, S., Hirota, M., Hoorn, C., Josse, C., Lapola, D. M., Larrea, C., Larrea-Alcazar, D. M., Lehm Ardaya, Z., Malhi, Y., Marengo, J. A., Melack, J., Moraes, R. M., Moutinho, P., Murmis, M. R., Neves, E. G., Paez, B., Painter, L., Ramos, A., Rosero-Peña, M. C., Schmink, M., Sist, P., ter Steege, H., Val, P., van der Voort, H., Varese, M., and Zapata-Ríos, G., United Nations Sustainable Development Solutions Network, New York, USA, https://doi.org/10.55161/VNBV7494, 2021c.

Gatti, L., Cunha, C., Cassol, H., Messias, C., Basso, L., Soler, L., Almeida, C., Domingues, L., Denning, S., Miller, J., Gloor, M., Correia, C., and Tejada, G.: Amazon carbon emissions double mainly by dismantled in law enforcement, Research Square [preprint], https://doi.org/10.21203/RS.3.RS-2023624/V1, 2022.

Giglio, L., Boschetti, L., Roy, D. P., Humber, M. L., and Justice, C. O.: The Collection 6 MODIS burned area mapping algorithm and product, Remote Sens. Environ., 217, 72–85, https://doi.org/10.1016/j.rse.2018.08.005, 2018.

Gloor, E., Wilson, C., Chipperfield, M. P., Chevallier, F., Buermann, W., Boesch, H., Parker, R., Somkuti, P., Gatti, L. V., Correia, C., Domingues, L. G., Peters, W., Miller, J., Deeter, M. N., and Sullivan, M. J. P.: Tropical land carbon cycle responses to 2015/16 El Niño as recorded by atmospheric greenhouse gas and remote sensing data, Philos. T. Roy. Soc. B, 373, 20170302, https://doi.org/10.1098/RSTB.2017.0302, 2018.

Gloor, M., Brienen, R. J. W., Galbraith, D., Feldpausch, T. R., Schöngart, J., Guyot, J. L., Espinoza, J. C., Lloyd, J., and Phillips, O. L.: Intensification of the Amazon hydrological cycle over the last two decades, Geophys. Res. Lett., 40, 1729–1733, https://doi.org/10.1002/GRL.50377, 2013.

Haghtalab, N., Moore, N., Heerspink, B. P., and Hyndman, D. W.: Evaluating spatial patterns in precipitation trends across the Amazon basin driven by land cover and global scale forcings, Theor. Appl. Climatol., 140, 411–427, https://doi.org/10.1007/s00704-019-03085-3, 2020.

Hansen, M. C., Potapov, P. V., Moore, R., Hancher, M., Turubanova, S. A., Tyukavina, A., Thau, D., Stehman, S. V., Goetz, S. J., Loveland, T. R., Kommareddy, A., Egorov, A., Chini, L., Justice, C. O., and Townshend, J. R. G.: High-Resolution Global Maps of 21st-Century Forest Cover Change, Science, 342, 850–853, https://doi.org/10.1126/science.1244693, 2013.

Hersbach, H., Bell, B., Berrisford, P., Hirahara, S., Horányi, A., Muñoz-Sabater, J., Nicolas, J., Peubey, C., Radu, R., Schepers, D., Simmons, A., Soci, C., Abdalla, S., Abellan, X., Balsamo, G., Bechtold, P., Biavati, G., Bidlot, J., Bonavita, M., Chiara, G., Dahlgren, P., Dee, D., Diamantakis, M., Dragani, R., Flemming, J., Forbes, R., Fuentes, M., Geer, A., Haimberger, L., Healy, S., Hogan, R. J., Hólm, E., Janisková, M., Keeley, S., Laloyaux, P., Lopez, P., Lupu, C., Radnoti, G., Rosnay, P., Rozum, I., Vamborg, F., Villaume, S., and Thépaut, J.: The ERA5 global reanalysis, Q. J. Roy. Meteor. Soc., 146, 1999–2049, https://doi.org/10.1002/qj.3803, 2020.

Hersbach, H., Bell, B., Berrisford, P., Biavati, G., Horányi, A., Muñoz Sabater, J., Nicolas, J., Peubey, C., Radu, R., Rozum, I., Schepers, D., Simmons, A., Soci, C., Dee, D., and Thépaut, J.-N.: ERA5 monthly averaged data on single levels from 1940 to present, Copernicus Climate Change Service (C3S) Climate Data Store (CDS) [data set], https://doi.org/10.24381/cds.f17050d7, 2023.

Hoesly, R. M., Smith, S. J., Feng, L., Klimont, Z., Janssens-Maenhout, G., Pitkanen, T., Seibert, J. J., Vu, L., Andres, R. J., Bolt, R. M., Bond, T. C., Dawidowski, L., Kholod, N., Kurokawa, J.-I., Li, M., Liu, L., Lu, Z., Moura, M. C. P., O'Rourke, P. R., and Zhang, Q.: Historical (1750–2014) anthropogenic emissions of reactive gases and aerosols from the Community Emissions Data System (CEDS), Geosci. Model Dev., 11, 369–408, https://doi.org/10.5194/gmd-11-369-2018, 2018.

Hubau, W., Lewis, S. L., Phillips, O. L., Affum-Baffoe, K., Beeckman, H., Cuní-Sanchez, A., Daniels, A. K., Ewango, C. E. N., Fauset, S., Mukinzi, J. M., Sheil, D., Sonké, B., Sullivan, M. J. P., Sunderland, T. C. H., Taedoumg, H., Thomas, S. C., White, L. J. T., Abernethy, K. A., Adu-Bredu, S., Amani, C. A., Baker, T. R., Banin, L. F., Baya, F., Begne, S. K., Bennett, A. C., Benedet, F., Bitariho, R., Bocko, Y. E., Boeckx, P., Boundja, P., Brienen, R. J. W., Brncic, T., Chezeaux, E., Chuyong, G. B., Clark, C. J., Collins, M., Comiskey, J. A., Coomes, D. A., Dargie, G. C., de Haulleville, T., Kamdem, M. N. D., Doucet, J.-L., Esquivel-Muelbert, A., Feldpausch, T. R., Fofanah, A., Foli, E. G., Gilpin, M., Gloor, E., Gonmadje, C., Gourlet-Fleury, S., Hall, J. S., Hamilton, A. C., Harris, D. J., Hart, T. B., Hockemba, M. B. N., Hladik, A., Ifo, S. A., Jeffery, K. J., Jucker, T., Yakusu, E. K., Kearsley, E., Kenfack, D., Koch, A., Leal, M. E., Levesley, A., Lindsell, J. A., Lisingo, J., Lopez-Gonzalez, G., Lovett, J. C., Makana, J.-R., Malhi, Y., Marshall, A. R., Martin, J., Martin, E. H., Mbayu, F. M., Medjibe, V. P., Mihindou, V., Mitchard, E. T. A., Moore, S., Munishi, P. K. T., Bengone, N. N., Ojo, L., Ondo, F. E., Peh, K. S.-H., Pickavance, G. C., Poulsen, A. D., Poulsen, J. R., Qie, L., Reitsma, J., Rovero, F., Swaine, M. D., Talbot, J., Taplin, J., Taylor, D. M., Thomas, D. W., Toirambe, B., Mukendi, J. T., Tuagben, D., Umunay, P. M., van der Heijden, G. M. F., Verbeeck, H., Vleminckx, J., Willcock, S., Wöll, H., Woods, J. T., and Zemagho, L.: Asynchronous carbon sink saturation in African and Amazonian tropical forests, Nature, 579, 80–87, https://doi.org/10.1038/s41586-020-2035-0, 2020.

Huffman, G. J., Adler, R. F., Morrissey, M. M., Bolvin, D. T., Curtis, S., Joyce, R., McGavock, B., and Susskind, J.: Global Precipitation at One-Degree Daily Resolution from Multisatellite Observations, J. Hydrometeorol., 2, 36–50, https://doi.org/10.1175/1525-7541(2001)002<0036:GPAODD>2.0.CO;2, 2001.

Justice, C. O., Townshend, J. R. G., Vermote, E. F., Masuoka, E., Wolfe, R. E., Saleous, N., Roy, D. P., and Morisette, J. T.: An overview of MODIS Land data processing and product status, Remote Sens. Environ., 83, 3–15, https://doi.org/10.1016/S0034-4257(02)00084-6, 2002.

Kaiser, J. W., Heil, A., Andreae, M. O., Benedetti, A., Chubarova, N., Jones, L., Morcrette, J.-J., Razinger, M., Schultz, M. G., Suttie, M., and van der Werf, G. R.: Biomass burning emissions estimated with a global fire assimilation system based on observed fire radiative power, Biogeosciences, 9, 527–554, https://doi.org/10.5194/bg-9-527-2012, 2012.

Kato, S., Rose, F. G., Rutan, D. A., Thorsen, T. J., Loeb, N. G., Doelling, D. R., Huang, X., Smith, W. L., Su, W., and Ham, S.-H.: Surface Irradiances of Edition 4.0 Clouds and

the Earth's Radiant Energy System (CERES) Energy Balanced and Filled (EBAF) Data Product, J. Climate, 31, 4501–4527, https://doi.org/10.1175/JCLI-D-17-0523.1, 2018.

Khatiwala, S., Primeau, F., and Hall, T.: Reconstruction of the history of anthropogenic CO_2 concentrations in the ocean, Nature, 462, 346–349, https://doi.org/10.1038/nature08526, 2009.

Koren, G., van Schaik, E., Araújo, A. C., Boersma, K. F., Gärtner, A., Killaars, L., Kooreman, M. L., Kruijt, B., van der Laan-Luijkx, I. T., von Randow, C., Smith, N. E., and Peters, W.: Widespread reduction in sun-induced fluorescence from the Amazon during the 2015/2016 El Niño, Philos. T. Roy. Soc. B, 373, 20170408, https://doi.org/10.1098/rstb.2017.0408, 2018.

Kruid, S., Macedo, M. N., Gorelik, S. R., Walker, W., Moutinho, P., Brando, P. M., Castanho, A., Alencar, A., Baccini, A., and Coe, M. T.: Beyond Deforestation: Carbon Emissions From Land Grabbing and Forest Degradation in the Brazilian Amazon, Front. For. Glob. Change, 4, 645282, https://doi.org/10.3389/ffgc.2021.645282, 2021.

Lan, X., Dlugokencky, E. J., Mund, J. W., Crotwell, A. M., Crotwell, M. J., Moglia, E., Madronich, M., Neff, D., and Thoning, K. W.: Atmospheric Carbon Dioxide Dry Air Mole Fractions from the NOAA GML Carbon Cycle Cooperative Global Air Sampling Network, 1968–2021, Version: 2022-11-21, Global Monitoring Laboratory [data set], https://doi.org/10.15138/wkgj-f215, 2022.

Lan, X., Tans, P., and Thoning, K. W.: Trends in globally-averaged CO_2 determined from NOAA Global Monitoring Laboratory measurements, Version 2023-04, Global Monitoring Laboratory [data set], https://doi.org/10.15138/9N0H-ZH07, 2023.

Lapola, D. M., Pinho, P., Barlow, J., Aragão, L. E. O. C., Berenguer, E., Carmenta, R., Liddy, H. M., Seixas, H., Silva, C. V. J., Silva-Junior, C. H. L., Alencar, A. A. C., Anderson, L. O., Armenteras, D., Brovkin, V., Calders, K., Chambers, J., Chini, L., Costa, M. H., Faria, B. L., Fearnside, P. M., Ferreira, J., Gatti, L., Gutierrez-Velez, V. H., Han, Z., Hibbard, K., Koven, C., Lawrence, P., Pongratz, J., Portela, B. T. T., Rounsevell, M., Ruane, A. C., Schaldach, R., da Silva, S. S., von Randow, C., and Walker, W. S.: The drivers and impacts of Amazon forest degradation, Science, 379, eabp8622, https://doi.org/10.1126/science.abp8622, 2023.

Lavric, J. and Walter, D.: Mole fractions of CO, CO_2, CH_4 (version 39.21.1178), Max Planck Institute for Biogeochemistry [data set], https://www.attodata.org/ddm/data/Showdata/39 (last access: 20 April 2023), 2022a.

Lavric, J. and Walter, D.: Mole fractions of CO, CO_2, CH_4 (version 64.9.1179), Max Planck Institute for Biogeochemistry [data set], https://www.attodata.org/ddm/data/Showdata/64 (last access: 20 April 2023), 2022b.

Lavric, J. and Walter, D.: Mole fractions of CO, CO_2, CH_4 (version 65.7.1180), Max Planck Institute for Biogeochemistry [data set], https://www.attodata.org/ddm/data/Showdata/65 (last access: 20 April 2023), 2022c.

Lavric, J. and Walter, D.: Mole fractions of CO, CO_2, CH_4 (version 66.7.1181), Max Planck Institute for Biogeochemistry [data set], https://www.attodata.org/ddm/data/Showdata/66 (last access: 20 April 2023), 2022d.

Lavric, J. and Walter, D.: Mole fractions of CO, CO_2, CH_4 (version 67.15.1182), Max Planck Institute for Biogeochemistry [data set], https://www.attodata.org/ddm/data/Showdata/67 (last access: 20 April 2023), 2022e.

Lavric, J. and Walter, D.: Mole fractions of CO, CO_2, CH_4 (version 68.7.1183), Max Planck Institute for Biogeochemistry [data set], https://www.attodata.org/ddm/data/Showdata/68 (last access: 20 April 2023), 2022f.

Lavric, J. and Walter, D.: Mole fractions of CO, CO_2, CH_4 (version 69.8.1184), Max Planck Institute for Biogeochemistry [data set], https://www.attodata.org/ddm/data/Showdata/69 (last access: 20 April 2023), 2022g.

Le Dimet, F.-X. and Talagrand, O.: Variational algorithms for analysis and assimilation of meteorological observations: theoretical aspects, Tellus A, 38A, 97–110, https://doi.org/10.1111/j.1600-0870.1986.tb00459.x, 1986.

Loeb, N. G., Doelling, D. R., Wang, H., Su, W., Nguyen, C., Corbett, J. G., Liang, L., Mitrescu, C., Rose, F. G., and Kato, S.: Clouds and the Earth's Radiant Energy System (CERES) Energy Balanced and Filled (EBAF) Top-of-Atmosphere (TOA) Edition-4.0 Data Product, J. Climate, 31, 895–918, https://doi.org/10.1175/JCLI-D-17-0208.1, 2018.

MapBiomas: Proyecto MapBiomas Amazonía – Colección [2.0] de los mapas anuales de cobertura y uso del suelo, MapBiomas, http://amazonia.mapbiomas.org/mapas-de-la-coleccion, last access: 8 July 2022.

Marengo, J. A., Espinoza, J.-C., Fu, R., Jimenez Muñoz, J. C., Muniz Alves, L., Ribeiro da Rocha, H., and Schongart, J.: Chapter 22: Long-term variability, extremes, and changes in temperature and hydro meteorology, in: Amazon Assessment Report 2021, edited by: Nobre, C., Encalada, A., Anderson, E., Roca Alcazar, F. H., Bustamante, M., Mena, C., Peña-Claros, M., Poveda, G., Rodriguez, J. P., Saleska, S., Trumbore, S., Val, A. L., Villa Nova, L., Abramovay, R., Alencar, A., Rodríguez Alzza, C., Armenteras, D., Artaxo, P., Athayde, S., Barretto Filho, H. T., Barlow, J., Berenguer, E., Bortolotto, F., Costa, F. A., Costa, M. H., Cuvi, N., Fearnside, P. M., Ferreira, J., Flores, B. M., Frieri, S., Gatti, L. V., Guayasamin, J. M., Hecht, S., Hirota, M., Hoorn, C., Josse, C., Lapola, D. M., Larrea, C., Larrea-Alcazar, D. M., Lehm Ardaya, Z., Malhi, Y., Marengo, J. A., Melack, J., Moraes, R. M., Moutinho, P., Murmis, M. R., Neves, E. G., Paez, B., Painter, L., Ramos, A., Rosero-Peña, M. C., Schmink, M., Sist, P., ter Steege, H., Val, P., van der Voort, H., Varese, M., and Zapata-Ríos, G., UN Sustainable Development Solutions Network, New York, USA, https://doi.org/10.55161/ZGJG8060, 2021.

Miller, J. B., Gatti, L. V., D'Amelio, M. T. S. S., Crotwell, A. M., Dlugokencky, E. J., Bakwin, P., Artaxo, P., and Tans, P. P. P.: Airborne measurements indicate large methane emissions from the eastern Amazon basin, Geophys. Res. Lett., 34, L10809, https://doi.org/10.1029/2006GL029213, 2007.

Miller, J. B., Martins, G. A., de Souza, R. A. F., and Schuldt, K. N.: Manaus aircraft profile data for the period 2017–2020; obspack_multi-species_1_manaus_profiles_v1.0_2021-05-20, NOAA Global Monitoring Laboratory [data set], https://doi.org/10.25925/20210519, 2021.

Morgenstern, O., Hegglin, M. I., Rozanov, E., O'Connor, F. M., Abraham, N. L., Akiyoshi, H., Archibald, A. T., Bekki, S., Butchart, N., Chipperfield, M. P., Deushi, M., Dhomse, S. S., Garcia, R. R., Hardiman, S. C., Horowitz, L. W., Jöckel, P., Josse, B., Kinnison, D., Lin, M., Mancini, E., Manyin, M. E., Marchand, M., Marécal, V., Michou, M., Oman, L. D., Pitari, G., Plummer, D. A., Revell, L. E., Saint-Martin, D., Schofield,

R., Stenke, A., Stone, K., Sudo, K., Tanaka, T. Y., Tilmes, S., Yamashita, Y., Yoshida, K., and Zeng, G.: Review of the global models used within phase 1 of the Chemistry–Climate Model Initiative (CCMI), Geosci. Model Dev., 10, 639–671, https://doi.org/10.5194/gmd-10-639-2017, 2017.

Naus, S., Domingues, L. G., Krol, M., Luijkx, I. T., Gatti, L. V., Miller, J. B., Gloor, E., Basu, S., Correia, C., Koren, G., Worden, H. M., Flemming, J., Pétron, G., and Peters, W.: Sixteen years of MOPITT satellite data strongly constrain Amazon CO fire emissions, Atmos. Chem. Phys., 22, 14735–14750, https://doi.org/10.5194/acp-22-14735-2022, 2022.

Nocedal, J.: Updating quasi-Newton matrices with limited storage, Math. Comput., 35, 773–782, https://doi.org/10.1090/S0025-5718-1980-0572855-7, 1980.

Patra, P. K., Houweling, S., Krol, M., Bousquet, P., Belikov, D., Bergmann, D., Bian, H., Cameron-Smith, P., Chipperfield, M. P., Corbin, K., Fortems-Cheiney, A., Fraser, A., Gloor, E., Hess, P., Ito, A., Kawa, S. R., Law, R. M., Loh, Z., Maksyutov, S., Meng, L., Palmer, P. I., Prinn, R. G., Rigby, M., Saito, R., and Wilson, C.: TransCom model simulations of CH_4 and related species: linking transport, surface flux and chemical loss with CH_4 variability in the troposphere and lower stratosphere, Atmos. Chem. Phys., 11, 12813–12837, https://doi.org/10.5194/acp-11-12813-2011, 2011.

Phillips, O. L. and Brienen, R. J. W.: Carbon uptake by mature Amazon forests has mitigated Amazon nations' carbon emissions, Carbon Balance Manag., 12, 1, https://doi.org/10.1186/s13021-016-0069-2, 2017.

Phillips, O. L., Aragão, L. E. O. C., Lewis, S. L., Fisher, J. B., Lloyd, J., López-González, G., Malhi, Y., Monteagudo, A., Peacock, J., Quesada, C. A., Van Der Heijden, G., Almeida, S., Amaral, I., Arroyo, L., Aymard, G., Baker, T. R., Bánki, O., Blanc, L., Bonal, D., Brando, P., Chave, J., De Oliveira, Á. C. A., Cardozo, N. D., Czimczik, C. I., Feldpausch, T. R., Freitas, M. A., Gloor, E., Higuchi, N., Jiménez, E., Lloyd, G., Meir, P., Mendoza, C., Morel, A., Neill, D. A., Nepstad, D., Patiño, S., Peñuela, M. C., Prieto, A., Ramírez, F., Schwarz, M., Silva, J., Silveira, M., Thomas, A. S., Steege, H. Ter, Stropp, J., Vásquez, R., Zelazowski, P., Dávila, E. A., Andelman, S., Andrade, A., Chao, K. J., Erwin, T., Di Fiore, A., Honorio, E. C., Keeling, H., Killeen, T. J., Laurance, W. F., Cruz, A. P., Pitman, N. C. A., Vargas, P. N., Ramírez-Angulo, H., Rudas, A., Salamão, R., Silva, N., Terborgh, J., and Torres-Lezama, A.: Drought sensitivity of the Amazon rainforest, Science, 323, 1344–1347, https://doi.org/10.1126/SCIENCE.1164033, 2009.

Potter, C. S.: Terrestrial Biomass and the Effects of Deforestation on the Global Carbon Cycle Results from a model of primary production using satellite observations, Bioscience, 49, 769–778, https://doi.org/10.2307/1313568, 1999.

Potter, C. S., Randerson, J. T., Field, C. B., Matson, P. A., Vitousek, P. M., Mooney, H. A., and Klooster, S. A.: Terrestrial ecosystem production: A process model based on global satellite and surface data, Global Biogeochem. Cy., 7, 811–841, https://doi.org/10.1029/93GB02725, 1993.

Randerson, J. T., van der Werf, G. R., Giglio, L., Collatz, G. J., and Kasibhatla, P. S.: Global Fire Emissions Database, Version 4.1 (GFEDv4), ORNL DAAC, Oak Ridge, Tennessee, USA [data set], https://doi.org/10.3334/ORNLDAAC/1293, 2017.

Ray, D., Nepstad, D., and Moutinho, P.: Micrometeorological and canopy controls of fire susceptibility in a forested Amazon landscape, Ecol. Appl., 15, 1664–1678, https://doi.org/10.1890/05-0404, 2005.

Silva, C. V., Aragao, L. E., Young, P. J., Espirito-Santo, F., Berenguer, E., Anderson, L. O., Brasil, I., Pontes-Lopes, A., Jerreira, J., Withey, K., França F., Graça, P. M. L. A, Kirsten, L., Xaud, H., Salimon, C., Scaranello, M. A., Castro, B., Seixas, M., Farias, R., and Barlow, J.: Estimating the multi-decadal carbon deficit of burned Amazonian forests, Environ. Res. Lett., 15, 114023, https://doi.org/10.1088/1748-9326/abb62c, 2020.

Silva Junior, C. H. L., Anderson, L. O., Silva, A. L., Almeida, C. T., Dalagnol, R., Pletsch, M. A. J. S., Penha, T. V., Paloschi, R. A., and Aragão, L. E. O. C.: Fire responses to the 2010 and 2015/2016 Amazonian droughts, Front. Earth Sci., 7, 97, https://doi.org/10.3389/feart.2019.00097, 2019.

Smallman, T. L., Milodowski, D. T., Neto, E. S., Koren, G., Ometto, J., and Williams, M.: Parameter uncertainty dominates C-cycle forecast errors over most of Brazil for the 21st century, Earth Syst. Dynam., 12, 1191–1237, https://doi.org/10.5194/esd-12-1191-2021, 2021.

Stephens, B. B., Gurney, K. R., Tans, P. P., Sweeney, C., Peters, W., Bruhwiler, L., Ciais, P., Ramonet, M., Bousquet, P., Nakazawa, T., Aoki, S., Machida, T., Inoue, G., Vinnichenko, N., Lloyd, J., Jordan, A., Heimann, M., Shibistova, O., Langenfelds, R. L., Steele, L. P., Francey, R. J., and Denning, A. S.: Weak northern and strong tropical land carbon uptake from vertical profiles of atmospheric CO_2, Science, 316, 1732–1735, https://doi.org/10.1126/science.1137004, 2007.

Takahashi, T., Sutherland, S. C., Wanninkhof, R., Sweeney, C., Feely, R. A., Chipman, D. W., Hales, B., Friederich, G., Chavez, F., Sabine, C., Watson, A., Bakker, D. C. E., Schuster, U., Metzl, N., Yoshikawa-Inoue, H., Ishii, M., Midorikawa, T., Nojiri, Y., Körtzinger, A., Steinhoff, T., Hoppema, M., Olafsson, J., Arnarson, T. S., Tilbrook, B., Johannessen, T., Olsen, A., Bellerby, R., Wong, C. S., Delille, B., Bates, N. R., and de Baar, H. J. W.: Climatological mean and decadal change in surface ocean pCO_2, and net sea–air CO_2 flux over the global oceans, Deep-Sea Res. Pt. II, 56, 554–577, https://doi.org/10.1016/j.dsr2.2008.12.009, 2009.

University of East Anglia Climatic Research Unit and Harris, I. C.: CRU JRA v1.1: A forcings dataset of gridded land surface blend of Climatic Research Unit (CRU) and Japanese reanalysis (JRA) data, January 1901–December 2017, 25 February 2019, Centre for Environmental Data Analysis [data set], https://doi.org/10.5285/13f3635174794bb98cf8ac4b0ee8f4ed, 2019.

van der Laan-Luijkx, I. T., van der Velde, I. R., Krol, M. C., Gatti, L. V., Domingues, L. G., Correia, C. S. C., Miller, J. B., Gloor, M., van Leeuwen, T. T., Kaiser, J. W., Wiedinmyer, C., Basu, S., Clerbaux, C., and Peters, W.: Response of the Amazon carbon balance to the 2010 drought derived with Carbon Tracker South America, Global Biogeochem. Cy., 29, 1092–1108, https://doi.org/10.1002/2014GB005082, 2015.

van der Werf, G. R., Randerson, J. T., Giglio, L., Collatz, G. J., Mu, M., Kasibhatla, P. S., Morton, D. C., DeFries, R. S., Jin, Y., and van Leeuwen, T. T.: Global fire emissions and the contribution of deforestation, savanna, forest, agricultural, and

peat fires (1997–2009), Atmos. Chem. Phys., 10, 11707–11735, https://doi.org/10.5194/acp-10-11707-2010, 2010.

van der Werf, G. R., Randerson, J. T., Giglio, L., van Leeuwen, T. T., Chen, Y., Rogers, B. M., Mu, M., van Marle, M. J. E., Morton, D. C., Collatz, G. J., Yokelson, R. J., and Kasibhatla, P. S.: Global fire emissions estimates during 1997–2016, Earth Syst. Sci. Data, 9, 697–720, https://doi.org/10.5194/essd-9-697-2017, 2017.

van Schaik, E., Killaars, L., Smith, N. E., Koren, G., van Beek, L. P. H., Peters, W., and van der Laan-Luijkx, I. T.: Changes in surface hydrology, soil moisture and gross primary production in the Amazon during the 2015/2016 El Niño, Philos. T. Roy. Soc. B, 373, 20180084, https://doi.org/10.1098/rstb.2018.0084, 2018.

Vermote, E. F., El Saleous, N. Z., and Justice, C. O.: Atmospheric correction of MODIS data in the visible to middle infrared: first results, Remote Sens. Environ., 83, 97–111, https://doi.org/10.1016/S0034-4257(02)00089-5, 2002.

Wilson, C., Chipperfield, M. P., Gloor, M., and Chevallier, F.: Development of a variational flux inversion system (INVICAT v1.0) using the TOMCAT chemical transport model, Geosci. Model Dev., 7, 2485–2500, https://doi.org/10.5194/gmd-7-2485-2014, 2014.

Wilson, C., Gloor, M., Gatti, L. V., Miller, J. B., Monks, S. A., McNorton, J., Bloom, A. A., Basso, L. S., and Chipperfield, M. P.: Contribution of regional sources to atmospheric methane over the Amazon Basin in 2010 and 2011, Global Biogeochem. Cy., 30, 400–420, https://doi.org/10.1002/2015GB005300, 2016.

Wilson, C., Chipperfield, M. P., Gloor, M., Parker, R. J., Boesch, H., McNorton, J., Gatti, L. V., Miller, J. B., Basso, L. S., and Monks, S. A.: Large and increasing methane emissions from eastern Amazonia derived from satellite data, 2010–2018, Atmos. Chem. Phys., 21, 10643–10669, https://doi.org/10.5194/acp-21-10643-2021, 2021.

Zheng, B., Chevallier, F., Yin, Y., Ciais, P., Fortems-Cheiney, A., Deeter, M. N., Parker, R. J., Wang, Y., Worden, H. M., and Zhao, Y.: Global atmospheric carbon monoxide budget 2000–2017 inferred from multi-species atmospheric inversions, Earth Syst. Sci. Data, 11, 1411–1436, https://doi.org/10.5194/essd-11-1411-2019, 2019.